

Seeding High Redshift QSOs by Collisional Runaway in Primordial Star Clusters

Harley Katz^{1*}, Debora Sijacki¹ and Martin G. Haehnelt¹

¹*Institute of Astronomy and Kavli Institute for Cosmology, University of Cambridge, Madingley Road, Cambridge, CB3 0HA*

16 July 2018

ABSTRACT

We study how runaway stellar collisions in high-redshift, metal-poor star clusters form very massive stars (VMSs) that can directly collapse to intermediate-mass black holes (IMBHs). We follow the evolution of a pair of neighbouring high-redshift mini-haloes with high-resolution, cosmological hydrodynamical zoom-in simulations using the adaptive mesh refinement code RAMSES combined with the non-equilibrium chemistry package KROME. The first collapsing mini-halo is assumed to enrich the central nuclear star cluster (NSC) of the other to a critical metallicity, sufficient for Population II (Pop. II) star formation at redshift $z \approx 27$. Using the spatial configuration of the flattened, asymmetrical gas cloud forming in the core of the metal enriched halo, we set the initial conditions for simulations of an initially non-spherical star cluster with the direct summation code NBODY6 which are compared to about 2000 NBODY6 simulations of spherical star clusters for a wide range of star cluster parameters. The final mass of the VMS that forms depends strongly on the initial mass and initial central density of the NSC. For the initial central densities suggested by our RAMSES simulations, VMSs with mass $> 400 M_{\odot}$ can form in clusters with stellar masses of $\approx 10^4 M_{\odot}$, and this can increase to well over $1000 M_{\odot}$ for more massive and denser clusters. The high probability we find for forming a VMS in these mini-haloes at such an early cosmic time makes collisional runaway of Pop. II star clusters a promising channel for producing large numbers of high-redshift IMBHs that may act as the seeds of supermassive black holes.

Key words: galaxies: high-redshift – quasars: supermassive black holes – galaxies: star clusters: general.

1 INTRODUCTION

The most simple path to a black hole is the death of a massive star of mass $M > 8 M_{\odot}$; however, these stellar mass black holes cannot accrete matter fast enough to produce the population of observed supermassive black holes (SMBHs) at high redshift if growth is limited to the Eddington rate (Volonteri et al. 2003; Volonteri & Rees 2005; Haiman 2006; Lodato & Natarajan 2006). The problem would be somewhat alleviated if Population III (Pop. III) stars were hundreds of solar masses as early simulations predicted (Bromm et al. 2002). Direct collapse of these stars into black holes of a similar mass could then provide a promising route to an SMBH if the resulting black hole remnants could be fed continuously. Recent, higher resolution simulations predict, however, that the masses of Pop. III stars are significantly lower due to fragmentation which

forms a small stellar association rather than an individual star. This casts doubt on the possibility that Pop. III stars produce massive black hole seeds (Greif et al. 2011). Even if Pop. III stars can reach masses of $\approx 1000 M_{\odot}$ (see e.g. Hirano et al. 2014), there are still major issues regarding the accretion once the black hole forms which are mainly due to radiative feedback (Johnson & Bromm 2007; Park & Ricotti 2011).

A different route to massive black hole seeds is the direct collapse of massive gaseous cores in the centres of atomic cooling haloes with $T_{\text{vir}} \gtrsim 10,000$ K at high redshift. In primordial galaxies that remain free from molecular hydrogen and metals, the gas cools very inefficiently at lower temperatures than the atomic cooling limit and matter will continue to accrete on to the central object at a high rate. Simulations indicate that the gas may then directly collapse into a black hole of $\approx 10^4 - 10^6 M_{\odot}$ (Loeb & Rasio 1994; Eisenstein & Loeb 1995; Begelman et al. 2006; Regan & Haehnelt 2009; Choi et al.

* E-mail: hk380@ast.cam.ac.uk

2013). This mechanism struggles, however, if the gas can efficiently fragment and cool and it is essential that the halo remains free from metal, dust, and H_2 contamination.

Simulations of the direct collapse scenario therefore invoke a strong, uniform, Lyman-Werner (LW) background to dissociate H_2 (Wolcott-Green et al. 2011). The most likely environment to find such a strong LW background is in the vicinity of a much larger host galaxy which has already undergone significant Pop. II or Pop. III star formation. There is some debate about the amplitude of the LW background required to suppress fragmentation (see e.g. Shang et al. 2010; Wolcott-Green & Haiman 2011; Sugimura et al. 2014; Latif et al. 2014b,c; Regan et al. 2014b) especially in the presence of cosmic ray and X-ray radiation (Inayoshi & Omukai 2011; Inayoshi & Tanaka 2014). Recently, Regan et al. (2014b) have shown that if the LW background is not uniform, the critical value needed to dissociate the H_2 is much higher than that for a uniform background. Latif et al. (2014a) suggest that when modelling the radiation spectra of Pop. II stars correctly and including the impact of X-ray ionization, the number density of direct collapse black holes decreases below that required to grow observed high-redshift SMBHs. X-ray feedback from the initial gas accretion on the black hole may further limit how massive such an object can grow in a short period of time (Aykutalp et al. 2014). Thus, it appears prudent to explore other mechanisms for forming massive black hole seeds at high redshift.

In this work, we study how stellar collisions in high-redshift, dense star clusters lead to the runaway growth of a single star. As stars collide, the mass and radius increase which boosts the probability for future collisions. This process becomes remarkably unstable, and analytic work, as well as simulations, demonstrates that, under the right conditions, runaway stellar collisions can produce a very massive star (VMS) that may collapse to an intermediate-mass black hole (IMBH) of $\approx 1000 M_\odot$ (Begelman & Rees 1978; Portegies Zwart et al. 2004; Freitag et al. 2006). For this reason, high-redshift nuclear star clusters (NSCs) are very promising candidates for the formation of IMBHs (Omukai et al. 2008). Devecchi & Volonteri (2009) used analytical models to demonstrate how a population of IMBHs might form in clusters at the centres of high-redshift galaxies. Runaway collisions in Pop. II star clusters may therefore be key for explaining the presence of black holes over the entire observed mass range.

Here, we use a combination of hydrodynamic simulations and direct summation, N -body simulations to model collisional runaway in dense stellar clusters at high redshift. In Part I (Section 2), we begin with self-consistent cosmological simulations performed with the RAMSES code and identify dense baryonic clumps in protogalaxies for which we can determine detailed chemo-thermodynamical properties. In Part II (Section 3), we extract the clumps from the cosmological simulations and populate them with stars, varying the stellar initial mass function (IMF) as well as a range of other parameters, and use this as the initial conditions for direct N -body simulations performed with NBODY6. Our model is nearly self-consistent, barring the ability to resolve the formation of individual stars within the cosmological framework, which is only now becoming possible (Safranek-Shrader et al. 2014).

2 PART I: COSMOLOGICAL HYDRODYNAMIC SIMULATIONS

2.1 Set-up of the cosmological simulations

2.1.1 Hydrodynamic, gravity, and chemistry solver

We use the publicly available adaptive mesh refinement (AMR) code RAMSES (Teyssier 2002) to follow the detailed hydrodynamics of the first collapsing objects at high redshift. We have replaced the default cooling module in RAMSES with the non-equilibrium chemistry solver KROME^{1,2} (Grassi et al. 2014). KROME uses the high-order DLSODES solver to solve the rate equations for the chemistry network. We follow the detailed abundances of 12 species: H , e^- , H^+ , H^- , He , He^+ , He^{++} , H_2 , H_2^+ , D , D^+ , and HD for the reactions listed in the KROME react.primordial-photoH2 network. Cooling due to metals via line transitions is included at $T < 10^4$ K for O I, C II, Si II, and Fe II. The abundances of these species are pinned to the hydrogen density in each cell assuming a metallicity which can change throughout the simulation. This is further described in Section 2.2.1. We emphasize that we do not assume an amplified LW background that would dissociate H_2 molecules and thus prevent cooling below $\approx 10^4$ K and inhibit gas fragmentation.

2.1.2 Optimizing resolution and refinement

For the purpose of our work, it is important to choose a large enough cosmological box to have a sufficiently massive halo forming within. At the same time, we need to choose the maximum level of refinement of the simulation such that we can resolve high enough densities for star formation to occur while at the same time making sure that no numerical fragmentation happens. Lada et al. (2010) suggest that star formation can begin to occur at volume number densities $n \gtrsim 10^4 \text{ cm}^{-3}$. Ceverino et al. (2010) argue that the Jeans length, λ_j , must be resolved by at least $N_j = 7$ cells at the maximum level of refinement, l_{max} , to prevent numerical fragmentation. Note that this is higher than the often used value of $N_j = 4$ cells suggested by Truelove et al. (1997). To study the properties of the birth clouds of NSCs that form in our simulations, we must evolve the simulations past the point of first collapse which makes these simulations susceptible to numerical fragmentation (Robertson & Kravtsov 2008; Ceverino et al. 2010; Prieto et al. 2013). In order to prevent this, we implement an artificial temperature floor based on the Jeans criteria at the maximum level of refinement,

$$T_{\text{floor}} = \frac{GN_j^2 \mu m_p \rho L^2}{\pi \gamma k_b 2^{2l_{\text{max}}}}. \quad (1)$$

Here, L is the physical length of the box at the redshift of interest, γ is the adiabatic index, N_j is the number cells we wish to resolve the Jeans length with, μ is the mean molecular weight, ρ is the mass density of the cell, k_b is the Boltzmann constant, and l_{max} is the maximum level of refinement. We set $N_j = 8$, double the number suggested by Truelove et al. (1997) and slightly larger than

¹ www.kromepackage.org

² <https://bitbucket.org/tgrassi/krome>

the value suggested by Ceverino et al. (2010). The minimum temperature of our simulation is governed by the physical temperature floor set by the cosmic microwave background (CMB) temperature at a given redshift. Thus, as long as $T_{\text{floor}} \lesssim 2.725(1+z)$ K, we will continue to accurately resolve the chemical and hydrodynamical properties of the gas. Inserting $T_{\text{floor}} \lesssim 2.725(1+z)$ K, $N_j = 8$, $n = 10^4 \text{ cm}^{-3}$, and $\mu = 1.22$ into equation (1), we see that we can safely resolve this density, choosing $L = 500$ comoving kpc h^{-1} at $z = 30$ with $l_{\text{max}} = 19$. For these values, $T_{\text{floor}} = 4.9$ K which is far below the temperature, $T_{\text{CMB}} = 84.5$ K, we expect the gas to cool to. At coarser levels $< l_{\text{max}}$, we refine in order to resolve the Jeans length by 16 cells, double our choice of N_j . In addition to these criteria, we have also implemented refinement criteria when the number of dark matter particles per cell becomes greater than 64 as well as when the baryons in the cell reach the equivalent scaled mass.

We emphasize that our choice of N_j is unlikely to be sufficient to resolve the turbulent properties of the gas on the scales that we simulate. Federrath et al. (2011) and Turk et al. (2012) demonstrate that in order to capture these properties in simulations, the Jeans length must be resolved by more than ≈ 32 cells especially in the presence of magnetic fields. As this is not the aim of our work and we only look to model the general structure and mass of the birth cloud of a high-redshift primordial star cluster, our choice of resolution should be sufficient.

2.1.3 Initial Conditions

We use the software package MUSIC (Hahn & Abel 2011) to construct initial conditions for a collisionless (dark-matter-only) simulation using second-order Lagrangian perturbations on a uniform grid at $z = 150$ with 256^3 particles in a 500 kpc h^{-1} comoving box. For the cosmological parameters, we assume the most recent values from Planck Collaboration et al. (2013) ($h = 0.6711$, $\Omega_m = 0.3175$, $\Omega_\Lambda = 0.6825$, $\sigma_8 = 0.8344$). The transfer function used to generate the initial conditions was created using CAMB (Lewis et al. 2000). We use the ROCKSTAR halo finder (Behroozi et al. 2013) to identify the most massive halo in our simulation at $z = 20$ which has a mass of $M_{\text{vir}} = 2.48 \times 10^7 M_\odot$. We define a cubic Lagrange region of side 127 comoving kpc to encompass all of the particles at $z = 20$ within a region much larger than the virial radius of the halo. Multiple dark-matter-only simulations were run until an atomic cooling halo with $T_{\text{vir}} \gtrsim 10^4$ K was identified at this redshift. An object of this mass is slightly overmassive for our choice of box size and represents an rms fluctuation of $> 4\sigma$ indicating that it is a rare halo. Such rare haloes are likely to be incorporated into the most massive galaxies at lower redshifts and are thus likely sites to host SMBHs at $z \gtrsim 6$ (Sijacki et al. 2009; Costa et al. 2014).

Baryons are introduced into the initial conditions using the local Lagrangian approximation at level 8 on the base grid, and both the dark matter and the baryons are initially placed at level 11 in the refinement region which gives an effective dark matter resolution of 2048^3 particles corresponding to particles of mass $m_{dm} = 1.08 M_\odot h^{-1}$. The initial level of the refined region was determined so that the mass of the dark matter particle does not subject the refined cells to N -body heating which can occur when the mass of

the dark matter particle is much greater than the mass of the cells. Various initial resolutions were tested and it was found that level 11 provides an efficient compromise between particle number and N -body heating effects which were found to be negligible at this level.

Although the high-resolution dark matter particles are unlikely to cause spurious heating, it is possible that low-resolution dark matter particles may infiltrate the refinement region and cause heating due to their much greater masses. We have checked throughout our simulation for contamination of low-resolution dark matter particles and found none of these particles within the virial radius of the haloes. The maximum level of refinement of our simulation was defined in Section 2.1.2 to be $l_{\text{max}} = 19$ so that the artificial temperature floor remains less than T_{CMB} at the redshifts of interest. This gives us a resolution of 0.95 comoving pc h^{-1} , corresponding to a physical resolution of 0.046 pc at $z = 30$.

2.1.4 Identifying the birth clouds of nuclear star clusters

We use the clump finder implemented in RAMSES to identify gravitationally contracting, bound clumps within the simulations. The clump finder is sensitive to a density threshold, a mass threshold, and a relevance threshold³. To identify a clump, we set the minimum density to be $(1+z)^3 \text{ cm}^{-3}$ which corresponds to $3 \times 10^4 \text{ cm}^{-3}$ at $z = 30$, and the relevance threshold to 1.5. We do not put a constraint on the minimum mass. We choose the density criteria slightly higher than the density we wish to resolve in order to minimize the chance of identifying spurious clumps at the density of interest. This algorithm is used only to identify the location of clumps within the simulation. In order to calculate clump properties, we perform a secondary analysis where we define the outer edge of the clump to be the radius where the average density drops below $n = 10^4 \text{ cm}^{-3}$. We only consider clumps with $N > N_j^3 = 512$ cells which are all at the highest level of refinement. For $l_{\text{max}} = 19$, the minimum volume of a clump is then 0.05 pc^3 at $z = 30$ which, assuming a spherical structure, sets a minimum radius of the clump to be $R_{\text{clump}} > 0.23 \text{ pc}$. The Arches cluster, the densest known star cluster in the local Universe with a central density of $\approx 10^5 M_\odot \text{ pc}^{-3}$, has an inner core radius of $\approx 0.2 \text{ pc}$ which is just about resolved by our simulation (Espinoza et al. 2009). This suggests that the full radius of high-density clusters will likely be sufficiently resolved out to their outer radii by our simulations.

2.1.5 When to end the simulation?

We end the simulation when high-mass stars are likely to form as these eventually disrupt the cluster by supernova feedback. We apply the following criteria to determine when a clump is populated with high-mass stars. For a given stellar IMF, $dN/dM = \xi(M)$, the total number of stars above a certain threshold mass, M_{thresh} , is given by $N_*(> M_{\text{thresh}}) = \int_{M_{\text{thresh}}}^{M_{\text{max}}} \xi(M) dM$. The main-sequence lifetime of stars as a function of their mass begins to flatten for stars

³ The relevance threshold is the ratio of the density peak to the maximum saddle density (Bleuler & Teyssier 2014). Clumps which do not break this threshold are considered noise.

with $M \gtrsim 40 M_\odot$. For a metallicity of $Z = 10^{-4} Z_\odot$, this corresponds to a main-sequence lifetime of ≈ 5 Myr. Thus, we set $M_{\text{thresh}} = 40 M_\odot$. We can then compute the mass of the cluster, M_{clump} needed to have $N_*(> M_{\text{thresh}}) \geq 1$. For a Salpeter IMF ($\xi(M) \propto M^{-2.35}$), with $M_{\text{min}} = 0.1 M_\odot$ and $M_{\text{max}} = 100 M_\odot$, we find $M_{\text{clump}} = 1.3 \times 10^4 M_\odot$ for $N_*(> M_{\text{thresh}}) = 1$. Once the NSC in the simulation reaches this fiducial mass of $1.3 \times 10^4 M_\odot$, we allow the simulation to run for $t_{\text{lag}} = 3.5$ Myr before we extract the clump, consistent with Devecchi & Volonteri (2009). Note that the stellar IMF at high redshift is unknown and the chosen value of M_{clump} will change considerably based on the choice of IMF. However, given that our chosen value of M_{clump} is much lower than the masses of observed NSCs, this is a rather conservative assumption.

2.2 Results from the cosmological simulation

In order to model the formation of a Pop. II star cluster, we identify a collapsing cloud of gas in close vicinity to another already collapsed object. This allows for the first halo to undergo an episode of Pop. III star formation and enrich the surrounding gas, post supernova, to a level suitable for forming Pop. II stars. The secondary collapsing object, however, must be located at a sufficient distance such that the radiation feedback from the first episode of Pop. III star formation does not disrupt the collapse

2.2.1 The collapse of two mini-halos in close separation

A halo of $M_{\text{vir}} = 2.48 \times 10^7 M_\odot$ was identified at $z = 20$ in the dark-matter-only simulation with comoving box size $500 \text{ kpc } h^{-1}$. The member particles were traced back to the initial conditions where they were centred and the simulation was reinitialized with baryons. Within this larger halo, two mini-haloes were identified with a distance such that the first collapsing object can enrich the second with metals.

At the time of collapse, the first mini-halo has a virial mass $M_{\text{vir}} = 2.7 \times 10^5 M_\odot$, a virial radius $R_{\text{vir}} = 62 \text{ pc}$ and a baryon fraction of 14.2 per cent. This halo begins to collapse at $z = 31.6$ and is the first object to collapse in the entire simulation volume.

If we assume that the average mass of Pop. III stars is $40 M_\odot$ (Hosokawa et al. 2011), the average lifetime of the system prior to supernova explosion is 3.9 Myr (Schaerer 2002). We model the chemical enrichment from these first supernovae by implementing a metallicity floor of $10^{-4} Z_\odot$ at $z = 30.7$. While this choice of metallicity floor is arbitrary, a prerequisite for the formation of a Pop. II star cluster is that the halo be enriched to a metallicity above the critical metallicity for fragmentation. For dust-free gas, this value is approximately $10^{-4} Z_\odot$ (Schneider et al. 2012). Slightly higher metallicities are unlikely to significantly affect the hydrodynamics of the gas at the densities our simulations probe, because as we will see, the temperature of the gas in the second mini-halo reaches the CMB temperature floor which prevents further cooling. A slightly higher metallicity may only accelerate this process.

⁴ The virial radius is calculated assuming that the average density of the object equals $200\rho_{\text{crit}}$.

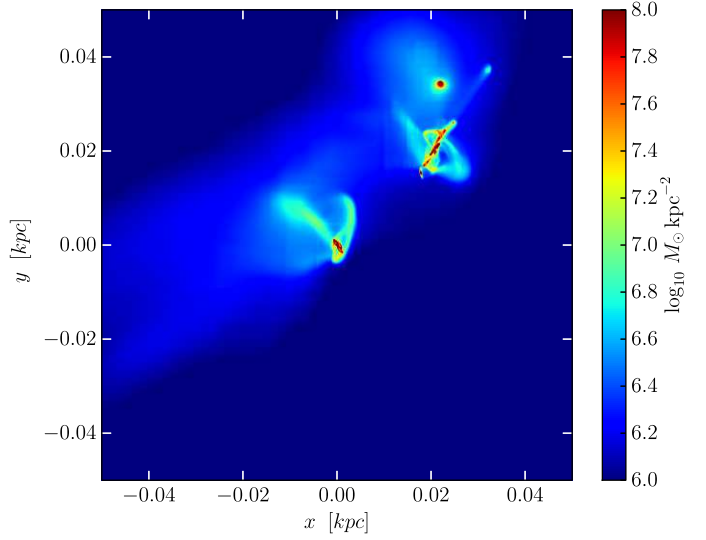


Figure 1. Snapshot showing the surface density in a 100 pc cube of the two mini-halos 8.5 Myr after the collapse of the second object. The secondary collapsing halo is centered.

The simulations of Ritter et al. (2012) model the transport of metals explicitly from the supernova of Pop. III stars and demonstrate that the surrounding medium can be enriched to metallicities as high as $10^{-2} Z_\odot$. The metal enrichment extends all the way to the virial radius of the halo in only 8.5 Myr. The outflow is expected to be bipolar and the dense filaments feeding the halo should be only minimally enriched. The first mini-halo studied here is less massive than the halo in Ritter et al. (2012). We may therefore expect more mixing along the filaments as the outflow should be less impeded by gas in the central regions of the halo in our simulation.

At $z = 28.9$, the second object begins its collapse at a distance of 117 pc from the centre of the first mini-halo and slightly outside its virial radius. This occurs 12.9 Myr after the collapse of the first object. This leaves sufficient time for the first object to form Pop. III stars and enrich the surrounding material with metals. The first mini-halo has since grown to $M_{\text{vir}} = 8.33 \times 10^5 M_\odot$ with $R_{\text{vir}} = 97 \text{ pc}$ and a baryon fraction of 16 per cent. The second object is falling into the potential well of the first mini-halo along a dense filament (see Fig. 1) and the two objects will eventually merge.

Assuming a population of $40 M_\odot$ Pop. III stars, we can estimate the expected intensity of the LW radiation at the location of the second mini-halo as,

$$J_{21} = 10^{21} \frac{\dot{N}_{\text{ph}} h_{\text{p}}}{4\pi^2 r^2}, \quad (2)$$

where J_{21} is in units of $10^{-21} \text{ erg cm}^{-2} \text{ s}^{-1} \text{ Hz}^{-1} \text{ sr}^{-1}$, $\dot{N}_{\text{ph}} = \bar{Q} N_* f_{\text{esc}}$ is the total number of photons emitted per second which escape the galaxy for a population of N_* Pop. III stars with mass of $40 M_\odot$, $\bar{Q} = 2.903 \times 10^{49} \text{ photons s}^{-1}$ (Schaerer 2002) for a $40 M_\odot$ Pop. III star, f_{esc} is the escape fraction, and h_{p} is Planck's constant. Assuming a maximal $f_{\text{esc}} = 1.0$ and a separation of 117 pc, we find $J_{21} = 9.37 N_*$.

Regan et al. (2014b) have demonstrated that for an anisotropic LW source, the critical value of J_{21} needed to completely dissociate H_2 and keep the gas from cooling is

$J_{21} \approx 10^3$. At a maximal escape fraction, complete dissociation would require the formation of a small cluster of roughly 100 Pop. III stars with masses of the order of $40 M_\odot$ at the centre of the first mini-halo whereas simulations of these mini-haloes tend to predict small stellar associations of Pop. III stars (Greif et al. 2011). Our simulations do not include dust which should be present in the second mini-halo and will help the gas cool and catalyse the formation of H_2 . One-zone models predict a lower critical value of J_{21} needed to disrupt the formation of HD which is the dominant coolant below ≈ 200 K (Yoshida et al. 2007; Wolcott-Green & Haiman 2011). This is because the main formation channel of HD, $H_2 + D^+ \rightarrow HD + H^+$, requires the presence of H_2 which is lowered by the exposure to the meta-galactic UV background. Given the low mass of the first mini-halo and the initial separation of the objects when the secondary collapses, it is unlikely that the radiative feedback from the first mini-halo will significantly disrupt the temperature and density evolution of the second. For these reasons, we do not include a meta-galactic UV background in our simulation. This approach is likely to be conservative as even a mild UV background can increase the accretion rate on to a central NSC (Devecchi & Volonteri 2009). Denser and more massive NSCs should more efficiently undergo runaway stellar collisions, and by neglecting a positive contribution from the UV background we may underestimate the final masses of the VMSs.

2.2.2 Evolution of the second mini-halo

In Fig. 2 (left and middle panels), we plot the mass-weighted phase space diagram of density versus temperature of the second minihalo within 10 pc of the densest cell just as it is collapsing at $z = 28.9$ and then 5 Myr later at $z = 28$. In these early phases of the collapse, cooling is dominated by H_2 lowers the gas temperature and the mass fraction of HD continues to rise at higher densities. HD and metals significantly contribute at higher densities until either the CMB temperature floor or the artificial temperature floor inhibits further cooling.

In the right-hand panel of Fig. 2, we show the phase space diagram at 14.3 Myr after the initial collapse. By this point in the simulation, much of the highest density gas has reached either T_{CMB} or is affected by the artificial temperature floor. One-zone models predict that the ratio $n_{\text{HD}}/n_{\text{H}_2}$ peaks around the maximum density we probe in this simulation before falling off steeply at higher densities. We do not probe these very high densities in our simulation and the HD abundance is forced to remain at a high value even though the gas should further collapse and lower the HD abundance. Some of the extra HD can diffuse out of the clump and lower the temperature of gas. This effect would cause an increase in fragmentation and decrease the mass of our central clump. With the inclusion of the CMB temperature floor, this effect is somewhat mitigated because the gas can only cool to T_{CMB} .

Because the small-scale fragmentation properties of the gas are subject to numerical resolution effects, we run two additional simulations in which we vary l_{max} between 18 and 20 and bracket our fiducial resolution. In Fig. 3, we plot the mass and density profiles of the halo computed using log-spaced bins centred on the centre of mass of the halo

for three different resolutions. At the time of collapse (left-most column), the mass and density profiles are well converged among the three different resolutions. By $z = 27.7$, a secondary clump begins to emerge in the higher resolution runs which appears as a bump in the density profile; however, the mass profile remains well converged. As the clumps begin to interact, we see some discrepancy between the different resolution runs in the very central regions; however, in all cases, the mass profile is well converged out to 1.5 pc. In Appendix A, we discuss how the small-scale differences and the formation of secondary clumps affect our results.

In Fig. 4, we return to the run with $l_{\text{max}} = 19$ and plot the evolution of the mass and radius of the clump as a function of time since initial collapse. Both properties increase linearly for ≈ 6 Myr until a second clump appears in the central regions of the mini-halo. The properties of the primary clump begin to oscillate as the presence of secondary fragments increases the average density at larger radii farther away from the centre. Despite this interaction, we can see in the top panel of Fig. 4 that the general trend is for the mass to increase. In order to obtain a smooth function for the mass of the clump as a function of time, we fit a piecewise linear model to the data points extracted directly from the simulation and set the break in the function to be the point where the oscillations begin. We apply this technique for both the mass and the radius of the clump of interest. Note that the radius remains relatively constant after the break.

10.8 Myr after the initial collapse, the central clump has grown to the threshold mass of $1.3 \times 10^4 M_\odot$. The average mass accretion on to the clump is $\dot{M}_{\text{clump}} \approx 6.0 \times 10^{-4} M_\odot \text{ yr}^{-1}$. The average mass of dark matter within the clump marginally decreases although this only affects the total mass accretion rate on to the clump by 5 per cent. At 14.3 Myr, which represents $0.8 \text{ Myr} + t_{\text{lag}}$, the clump reaches a mass of $1.77 \times 10^4 M_\odot$ within a radius of 1.25 pc.

2.2.3 Internal clump structure

We assume that the stars form in the highest density regions of the clump. We identify the densest simulations cells making up a certain fraction the total mass and define them to be star forming. For reasons described in Section 3.1.5, we set the star formation efficiency (SFE), $\epsilon = 2/3$. In Fig. 5, we plot the spatial distribution of these cells as viewed along the axis with the highest magnitude of angular momentum (J_z axis) for each of the three different resolution simulations within the star-forming radius of 1.25 pc from the densest cell at three different times. Tracing this region throughout the simulation, we see that at the time of initial collapse (top row of Fig. 5), all three resolutions exhibit a very similar spatial distribution. 5 Myr later (middle row of Fig. 5), the spatial distributions of the three simulations still agree reasonably well, but there is clear evidence that the higher resolution runs collapse further and we begin to see fragmentation. By 14.3 Myr, the distribution of the gas at the different refinement levels has completely diverged although the mass contained within the region remains reasonably consistent. The two higher resolution simulations have fragmented into multiple clumps while the $l_{\text{max}} = 18$ run contains only one object. Interactions between the different clumps in the runs with higher level of refinement

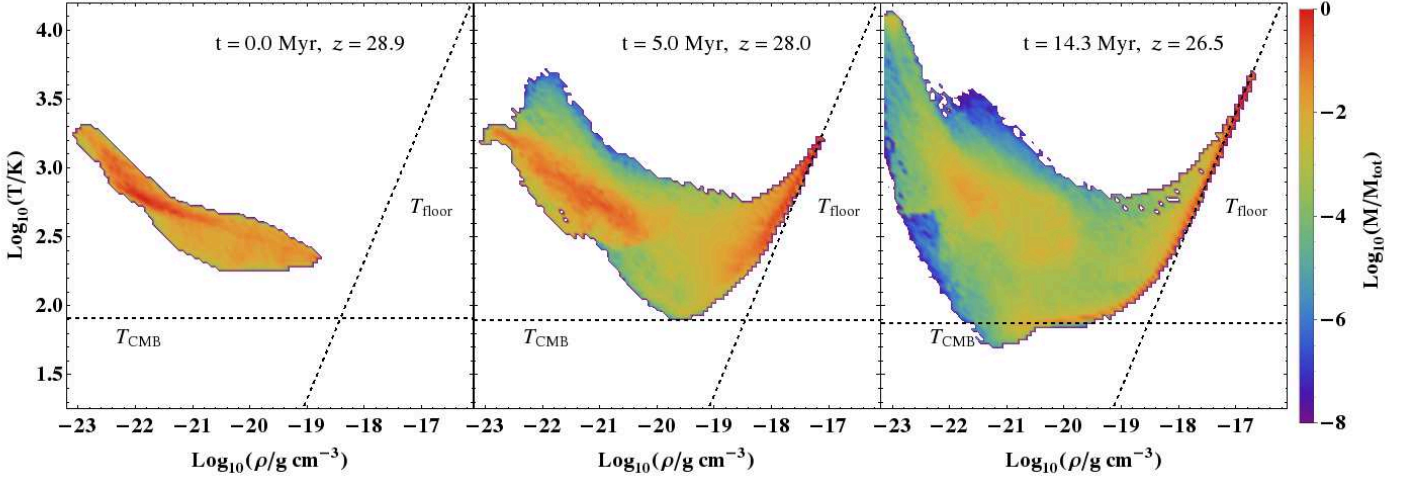


Figure 2. Mass-weighted phase space diagrams of density versus temperature at the initial collapse (*left*), 5 Myr after the collapse (*middle*), and 14.3 Myr after the collapse (*right*) which is the point at which we extract the clump properties from the simulation for input into direct N -body calculations. This includes all gas within 10 pc of the densest cell. The gas cools to a few hundred kelvin initially due to H_2 , cooling then reaches the CMB temperature floor due to HD and metal cooling. The dashed lines represent the CMB temperature floor and the artificial temperature floor as labelled.

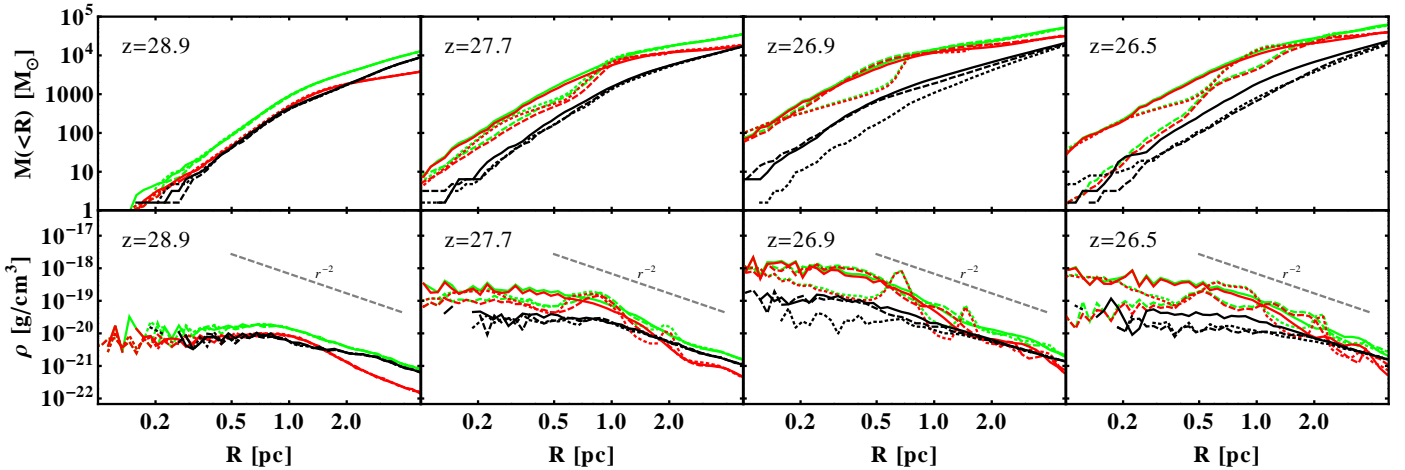


Figure 3. Enclosed mass profiles (*top*) and density profiles (*bottom*) for three different resolutions as a function of redshift. The dark matter, gas, and total profiles are represented by black, red, and green lines, respectively. The solid, dashed, and dotted lines represent $l_{\max} = 18, 19$, and 20 .

have caused a significant deviation in the dynamics in the central region which makes the structures appear different. As pointed out by Regan et al. (2014a), interpreting the results of AMR simulations at different refinement levels is non-trivial and choosing a refinement level that is either too high or too low can lead to misinterpretation of the overall dynamical evolution of collapse simulations. Our simulations indicate that fragmentation of the central clump is likely and therefore $l_{\max} = 19$ is the minimum resolution required in this study to resolve the central dynamics and this is the resolution we choose for further analysis.

We hence use the spatial structure identified in the $l_{\max} = 19$ RAMSES simulation to generate reasonably realistic initial conditions for NBODY6 simulations of the NSCs.

We caution here, however, that this approach is by no means unambiguous, and we aim to sample realistic rather than exact initial conditions. The resolution effects on the transition from the RAMSES to the NBODY6 simulations are further discussed in Appendix A where we demonstrate that regardless of which resolution is chosen between our two high-resolution runs, the masses of the VMSs which form remain consistent with each other.

For the run with our fiducial resolution with $l_{\max} = 19$, the total volume of cells which represent the densest $2/3$ of the total gas mass in the star-forming region is 0.109 pc^3 . In this simulation, we identify three distinct regions: a main central massive clump (clump 1), a less massive, off-centred clump (clump 2), and a further less massive, off-centred

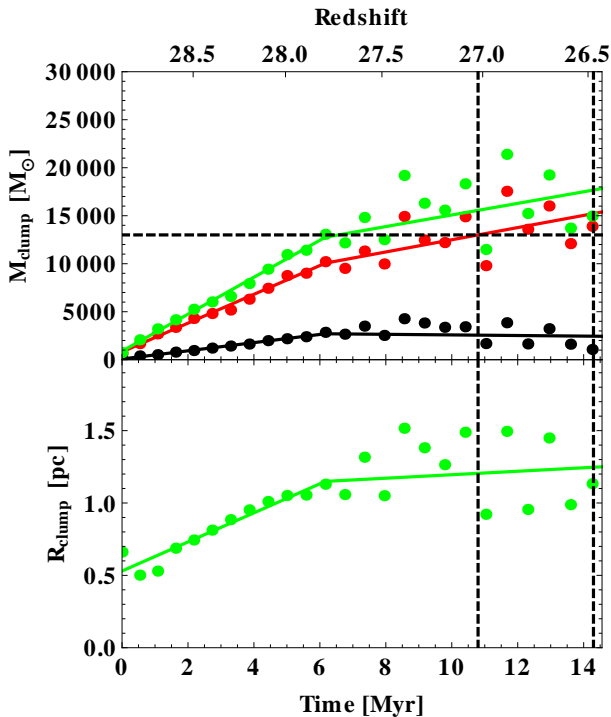


Figure 4. *Top.* Mass of the clump in the secondary collapsing object as a function of time since the initial collapse. The data points represent the simulations and the solid lines represent the fitting function described in the text. The black line shows the dark matter mass, the red line shows the gas mass, and the green line shows the total mass. The horizontal, dashed, black line represents the fiducial mass at which we expect the cluster to form high mass stars. The first vertical, dashed, black line is the time at which the clump reaches the fiducial mass and the second vertical, dashed, black line is 3.5 Myr after the first which is the point at which the clump mass is extracted. *Bottom.* Radius of the clump where the average density drops below 10^4 cm^{-3} as a function of time since the initial collapse. The dashed, black vertical lines are at the same times as in the top panel and a piecewise linear fit to the data is also shown.

clump (clump 3) as indicated in the bottom-middle panel of Fig. 5. The masses of these clumps are $9094.4 M_{\odot}$, $835.4 M_{\odot}$, and $170.4 M_{\odot}$, respectively. The structure, orientation, and relative velocities of these clumps are used in Part II of this work to generate a series of non-spherical initial conditions for direct N-body simulations.

3 PART II: DIRECT N-BODY SIMULATIONS

3.1 Setup of the NBODY6 simulations

3.1.1 From birth cloud to star cluster

To create initial conditions for the direct N-body simulations, a minimal bounding ellipsoid enclosing all of the cells for each of the individual regions shown in the bottom-

middle panel of Fig. 5 is computed⁵. We aim to create a set of star cluster initial conditions which have the same spatial structure and bulk velocity properties as the gas bounded by the three ellipsoids. The three clumps/star clusters will then be evolved together and allowed to interact. To construct flattened, ellipsoidal star clusters for each individual clump identified in the birth cloud, we first average the three primary axis lengths and then generate a spherical star cluster with this radius with MCLUSTER (Küpper et al. 2011). For each initial sphere, the axial ratios are scaled and the positions of individual stars are rotated and translated according to the properties of the ellipsoids to reproduce the shapes and orientation of the individual clumps with respect to each other. The velocities of individual stars are initialized by choosing a value of the virial parameter Q ($Q = 0.5$ represents a virialized cluster and $Q < 0.5$ represents dynamically cold clusters) for the initial spherical star cluster prior to axis scaling and the velocities are rotated to be consistent with the reorientation of the positions. We do not attempt to scale the magnitudes of the velocities and only vary Q for the initial spherical cluster which determines how dynamically cold the initial cluster is. The bulk velocities of clumps 2 and 3 with respect to clump 1 are calculated directly from the hydrodynamic simulation and added to the initial velocities of individual stars of clumps 2 and 3, but we do not include a net rotation for the central clump which may delay core collapse. The initial conditions for each of the individual clumps are then merged into one file to make a single input for NBODY6.

The initial density profile of the spherical star clusters, prior to axis scaling, is varied between a Plummer model (Plummer 1911) and a constant-density model. We further use the fractal dimension option of MCLUSTER to model inhomogeneous systems where stars are sub-clustered to account for the spatial inhomogeneity in real star-forming systems. $D = 3.0$ represents a cluster with no fractalization and $D = 1.6$ represents a very clumpy distribution (Goodwin & Whitworth 2004). We should note here that for both the Plummer and the fractal models not all stars in the initial conditions are placed within the bounding ellipsoid. Higher values of D effectively increase the initial volume that contains the stars and therefore lower the average initial densities.

The dark matter and gas not converted to stars are modelled as an external potential with a Plummer sphere and the virial radius is set to be 1.25 pc, matching that of the cosmological, hydrodynamic simulation. The initial mass of the external potential is $7524.7 M_{\odot}$ and this mass increases at a rate of $6.04 \times 10^{-4} M_{\odot} \text{ yr}^{-1}$ over the course of the simulations as measured from the RAMSES simulation to represent the gas and dark matter accretion on to the NSC. Accretion at this rather low rate affects the dynamics of the star cluster very little, but is, nevertheless, included for completeness. Note that accretion at higher rates could play an important role in the evolution of the cluster.

⁵ In addition to these three regions, there is a diffuse ring of mass located around the central clump and parallel to the J_z axis. The total mass in this ring is 5 per cent of the total mass in the main, central clump and we have included it in the mass we list for clump 1 but do not take into account its volume.

3.1.2 Gravity solver

The evolution of these embedded star clusters and the formation of VMSs from runaway stellar collisions are modelled with the GPUaccelerated version of NBODY6 (Aarseth 1999; Nitadori & Aarseth 2012). The minimum energy conservation requirement is set so $\Delta E/E \leq 10^{-3}$. Because the remaining gas and dark matter are modelled as a background potential which is variable as a function of the gas accretion and expulsion rates, energy is not strictly conserved.

3.1.3 Stellar evolution and metallicity effects

Stellar evolution for individual stars is modelled with the SSE and BSE packages (Hurley et al. 2000, 2002) built into NBODY6. All stars begin on the zero-age main sequence (ZAMS).

The lifetimes of the most massive stars are reasonably constant at $M > 40 M_\odot$, and range from $\approx 3.5 - 5$ Myr with decreasing mass. These values are rather independent of metallicity. At this epoch in the cluster lifetime, the most massive stars begin to undergo supernovae, a process which is not modelled in our simulations. For this reason, all simulations are stopped at 3.5 Myr when the first massive star evolves off the main sequence. Contrary to main-sequence lifetimes, radii of stars are heavily dependent on metallicity and only converge for lower mass stars. The stellar evolution package native to NBODY6 does not inherently sample the metallicity of our cluster.

The models of Baraffe et al. (2001) predict that stars with mass $M \approx 100 M_\odot$ and metallicity $Z = 10^{-4} Z_\odot$ have radii of roughly half that of the lowest metallicity native to NBODY6. We apply a correction term to the radii to account for this. At $M < 10 M_\odot$, all radii are as computed for the lowest metallicity available in NBODY6 and for $M > 10 M_\odot$, a linear interpolation is applied so that $100 M_\odot$ stars have a radius half that predicted by the stellar evolution packages.

Glebbeek et al. (2009) demonstrated that at high metallicity, stellar winds become the dominant mode of mass-loss from a star and can significantly limit the final remnant mass of a collision product. We have implemented the mass-loss rates of Vink et al. (1999, 2000, 2001) and apply them to the collisionally produced stars with $M > 100 M_\odot$. The strength of the wind scales with the metallicity. Lower metallicity stars undergo far less mass-loss than their higher metallicity counterparts. For the metallicity considered here, stellar winds are inefficient at decreasing the mass of the VMS over the main-sequence lifetimes of these stars. However, real NSCs are likely to exhibit a range in metallicities and this will become important if the metallicity of the cluster is significantly increased.

Another consequence of the decreased wind strength is the inability of the stars to unbind the gas from the cluster. This may decrease the number density of stars throughout the cluster. Using models from STARBURST99, (Leitherer et al. 1999), for a Salpeter stellar IMF with a maximum mass of $100 M_\odot$ and an instantaneous starburst, we can calculate the integrated mechanical luminosity of our star cluster by scaling the mass and $Z^{0.5}$. Our simple model assumes that the mechanical luminosity is dominated by winds rather than radiation. By comparing this energy input to the binding energy of the cluster, we find that the

energy input from the stars only becomes comparable to the binding energy of the cluster at ≈ 3.5 Myr which is the lifetime of the most massive stars in the cluster and the point at which we stop the simulations. This calculation also assumes that all of the mechanical luminosity couples to the gas efficiently. We can, therefore, safely neglect gas expulsion in our simulations.

3.1.4 Treatment of stellar collisions

As the simulations begin with all stars on the ZAMS and are truncated after 3.5 Myr, the only collisions which can occur are those between two main-sequence stars. A sticky sphere approximation is used so that if the distance between the centres of the two stars is less than the sum of the radii, it is assumed that the stars have merged. All of the stars in the simulations are on the main sequence and we assume that when stars collide, the remnant is also a main-sequence star. The new star is assumed to be well mixed and the new lifetime is given to be consistent with Tout et al. (1997). This results in a slight rejuvenation of the lifetime. If the collision product has $M > 100 M_\odot$, the resulting evolution is treated as a $100 M_\odot$ star.

Smoothed particle hydrodynamic simulations which have studied the merges of main-sequence stars have shown that not all of the mass that enters a collision is necessarily retained. The mass ratio of the stars, as well as the orientation of the collision, ranging from head on to grazing, influences the amount of mass that is lost (Trac et al. 2007; Dale & Davies 2006). Glebbeek et al. (2013) demonstrated that the mass-loss is also slightly dependent on the types of stars which merge. Since all stars in our simulations are on the main sequence, we adopt approximated mass-loss rates consistent with the high-mass half-age main-sequence merger models of Glebbeek et al. (2013) as follows:

$$dM = \min \left[0.062 \frac{M_2}{0.7 M_1}, 0.062 \right] (M_1 + M_2), \quad (3)$$

where M_1 is the mass of the primary and M_2 is the mass of the secondary. The mass-loss is roughly constant for all mass ratios with $M_2/M_1 > 0.7$. This is enforced in our equation. We only calculate this mass-loss when the stars collide almost head-on such that the distance between the two centres is less than half the sum of the two radii of the stars and when the orbital kinetic energy of the secondary star just prior to the collision is greater than the binding energy

3.1.5 Star formation efficiency

In the local Universe the SFE, $\epsilon = M_*/(M_* + M_g)$, is $\approx 10 - 30$ per cent (Lada & Lada 2003). However, we do not know whether this is applicable to the high-redshift Universe where the environment is very different. Dib et al. (2011) have demonstrated that the SFE increases exponentially with decreasing metallicity with no relation to the mass of the birth cloud. The metallicity studied in their work is three orders of magnitude greater than the metallicity floor of $10^{-4} Z_\odot$ used in this study which may suggest that the SFE in the NSC forming in our simulated galaxy could have $\epsilon \gg 35$ per cent. Simulations of Pfalzner & Kaczmarek (2013) show that, in order to reproduce characteristics of local compact clusters of similar mass to the NSC that forms

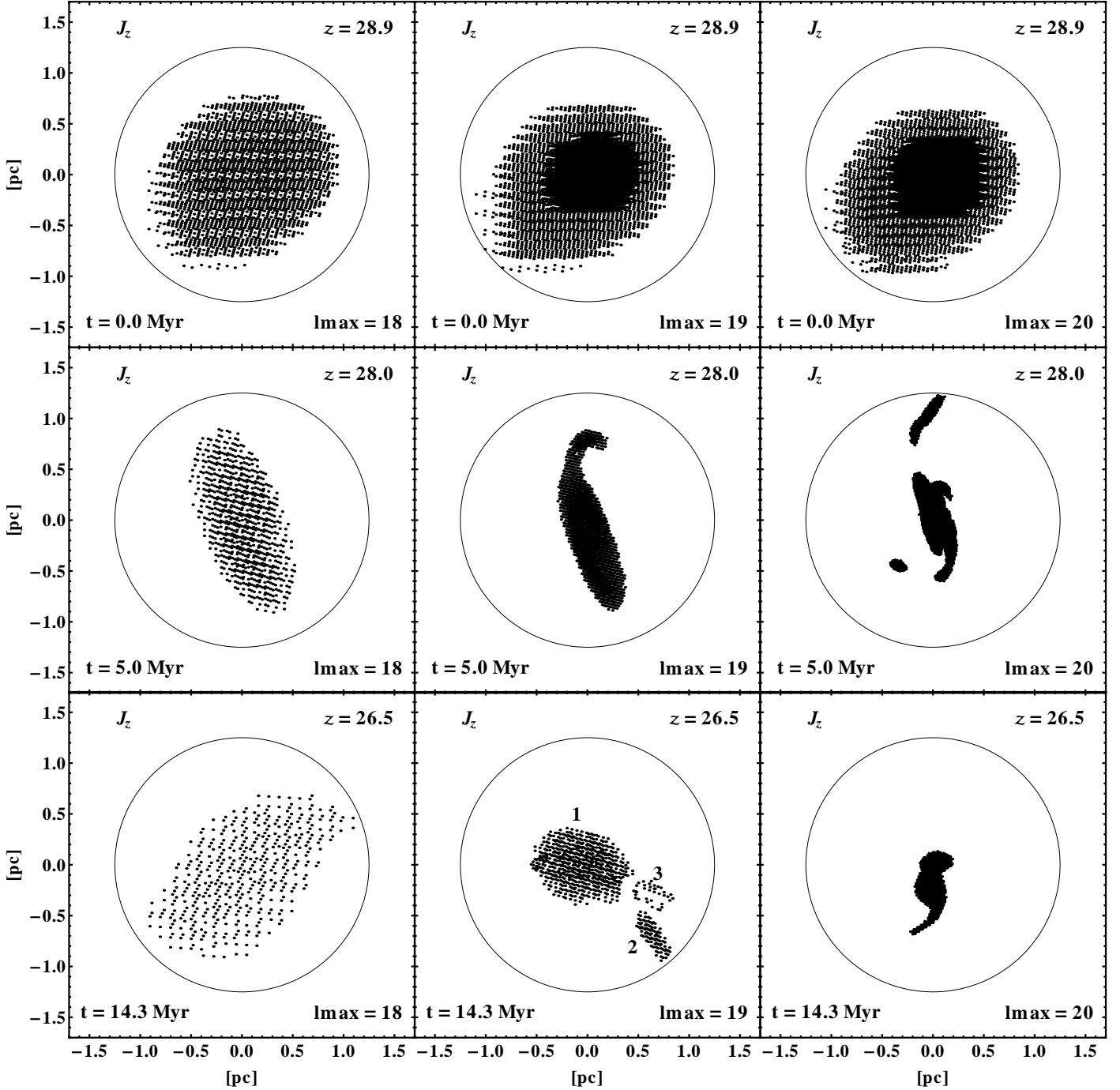


Figure 5. View along the J_z axis of the densest cells which represent $2/3$ of the total mass within a 1.25 pc radius of the densest cell for the three different resolutions (columns) and at three different times (rows). The top row shows the initial collapse, the middle row is 5 Myr after collapse, and the bottom row is 14.3 Myr after the collapse, the point at which we extract the clump properties. Points in the bottom row represent the corresponding star forming region of the clump. The three clumps labelled 1, 2, and 3 in the bottom middle panel represent the three clumps which were extracted from the $l_{\max} = 19$ simulation and used to create non spherical initial conditions for simulation with NBODY6. The circle indicates a radius of 1.25 pc.

in our simulation, SFEs of $60 - 70$ per cent need to be assumed. This finding is further supported by the simulations of Fujii (2014) which demonstrate that a local SFE of more than 50 per cent is needed for the formation of young massive clusters which have properties similar to such objects

in the local Universe. Both observations and the simulation results discussed suggest that it is indeed appropriate to assume a rather high SFE in our star cluster simulations.

For our fiducial model, we adopt $\epsilon = 2/3$ which is defined at the point at which we extract the clump properties

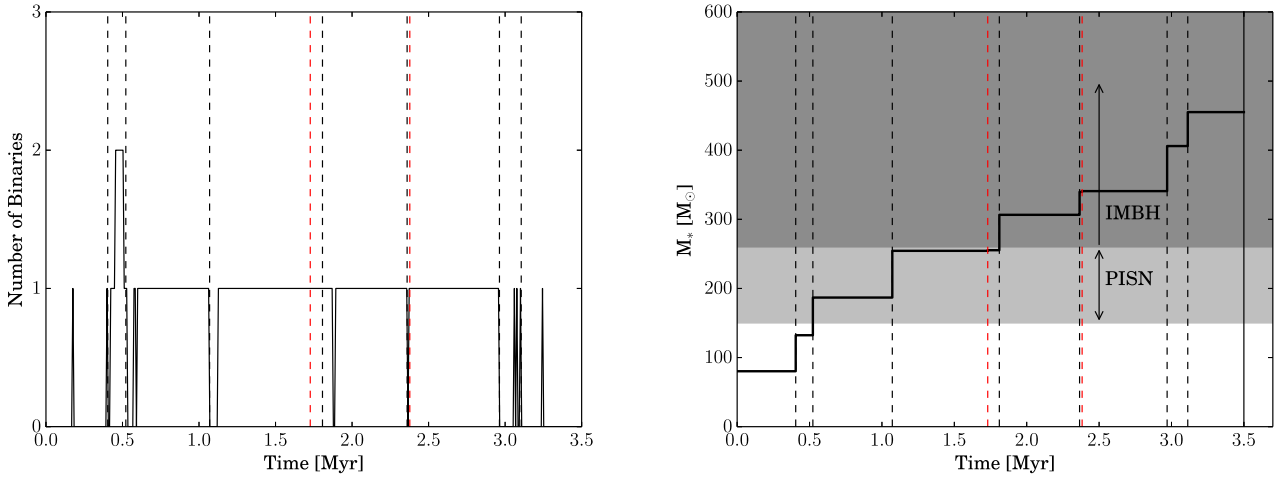


Figure 6. *Left.* Number of binaries as a function of time for a representative NBODY6 simulation with the top-heavy Salpeter IMF, with no initial binaries or primordial mass segregation, that results in a VMS with a mass of $M_{\text{VMS}} = 455.1 M_{\odot}$ after 9 separate collisions. The time at which the VMS undergoes a collision/merger is indicated with a vertical line where black represents a binary collision and red represents a hyperbolic collision. *Right.* The mass of the collisional runaway as a function of time for the same simulation. The solid vertical line is the lifetime of the most massive stars in the cluster and the point at which the simulation is stopped. The light and dark gray regions represent the mass ranges where PISNs and IMBHs potentially form. In each panel, the time at which the VMS underwent a collision/merger is indicated with a dashed vertical line where black represents a binary collision and red represents a hyperbolic collision.

in the simulation. We should note, however, that the SFE is dependent on how the edge of the clump is defined. This is not necessarily consistent between simulations and observations. We have chosen a fiducial density threshold of 10^4 cm^{-3} which is higher than the densities at the edges of many local molecular clouds. Since observations may probe lower densities, the SFE which we quote will appear higher than the true efficiency if a fair comparison would be made between observations and the simulation. For example, if we consider a sphere of radius 10 pc around the densest cell and consider only gas with $\rho \geq 10^2 \text{ H cm}^{-3}$, the effective SFE would be equivalent to 22 per cent.

Because mass is accreting on to the NSC, the SFE calculated at the beginning of the simulation is higher than it would be if calculated just prior to the most massive stars going supernova. With the mass accretion rate of $\dot{M}_{\text{clump}} = 6.0 \times 10^{-4} M_{\odot} \text{ yr}^{-1}$ taken from our RAMSES simulation, the effective SFE at the end of the N -body simulation drops to 57 per cent, 10 per cent lower than the initial value. The impact of varying the SFE on our results is further discussed in Appendix B where we relax the assumption of $\epsilon = 2/3$.

3.1.6 Possible outcomes of runaway collisions

There are three possible outcomes of the cluster evolution that we are interested in identifying: (1) when collisional runaway results in the formation of a VMS with $M > 260 M_{\odot}$, (2) when stellar collisions result in the formation of a pair-instability supernova (PISN) which occurs when mergers produce a star with $150 < M < 260 M_{\odot}$, and (3) when collisions do not lead to efficient runaway growth and no star exceeds the PISN mass threshold. In order to sample the probability of each outcome, we generate multiple realizations of each set of initial conditions.

The runaway collision process begins when the high-mass stars sink to the centre of the cluster and dynamically form binaries. Encounters with other stars perturb these binaries by either three- (or many-) body scattering or by binary exchanges. The semimajor axis of the dominant binary continues to shrink as the system loses energy due to these encounters and if the eccentricity becomes high enough, the two stars merge. This process of binary capture followed by a merge repeats until the core evolves to sufficiently low density or the supernovae from the first massive stars disrupt the cluster. To demonstrate this process in practice, we show in Fig. 6 the number of binaries as a function of time as well as the mass evolution of the collisional runaway star for a representative star cluster simulation which forms a VMS with a mass of $M_{\text{VMS}} = 455.1 M_{\odot}$ after nine separate collisions. We indicate the times of a collision and see that most of these coincide with the points at which the number of binaries changes. The two specific instances where the collision time is not related to a change in number of binaries occur when the VMS undergoes a hyperbolic collision. The masses of the secondary objects in these types of collision tend to be small with the average secondary mass of the hyperbolic collision being $1.05 M_{\odot}$ compared to the average mass of the secondary star in binary collisions being $56.2 M_{\odot}$. Hence, the hyperbolic collisions tend to contribute negligible amounts of mass to the overall mass of the VMS.

3.2 Results of the direct N -body simulations

3.2.1 Non-spherical N -body simulations

We begin by studying the non-spherical star clusters which are set up to reproduce the mass distribution obtained from the cosmological simulations

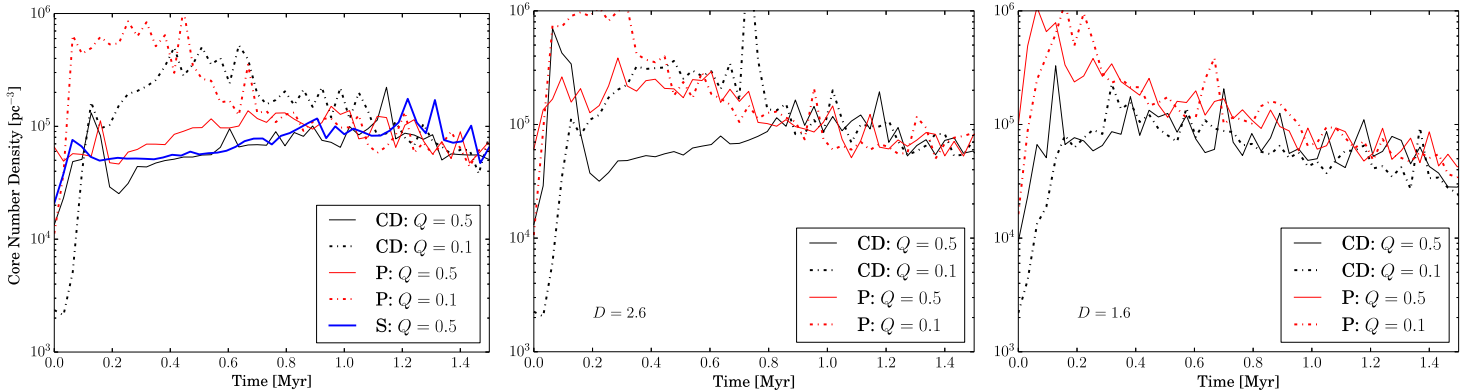


Figure 7. Initial evolution of the number density of the core as a function of time for models with $D = 3.0$ (left), $D = 2.6$ (middle), and $D = 1.6$ (right). Red lines represent models that were initialized with Plummer potentials (P) while black lines started at constant density (CD). Initial $Q = 0.5$ and $Q = 0.1$ are indicated by the solid and dot-dashed lines, respectively. The blue line in the left panel shows the evolution of a comparison spherical model (S) with $D = 3.0$, $Q = 0.5$, and $f_c = 0.5$.

3.2.1.1 Varying the density profile, Q and D In Table 1, we list the initial conditions of all of the models sampled in this section as well as the results. We fix the stellar IMF to a top-heavy⁶ Salpeter IMF (TH_Salp) such that $M_{\min} = 1 M_{\odot}$, $M_{\max} = 100 M_{\odot}$ and $\alpha = -2.35$. For each of these models, 50 realizations have been run. The fraction of models which produce a VMS does not exceed 12 per cent and the most massive VMSs have masses in the range 275-410 M_{\odot} . The average number of collisions for these models is rather low. This prohibits collisional runaway in the majority of realizations. In Fig. 7, we plot the core number density⁷ for this initial set of models and see that it increases extremely quickly within the first 0.25 Myr and slowly decreases thereafter. Even models which do not form VMSs exhibit this generic behaviour. This number density rarely peaks above 10^6 pc^{-3} and the final number density always converges to values of $\approx 2 \times 10^4 \text{ pc}^{-3}$ at $t = 3.5 \text{ Myr}$. Differences in the initial degree of fractalization have a very small effect on the core number density. The total number of collisions increases in the models with lower values of D . However, this does not affect the fraction of models which produce VMSs. This increase is likely to be due to a higher initial local number density in the more fractal models. There is a clear difference in the peak core number density between models which are initialized with a Plummer profile compared to those initialized with constant density. The Plummer models start with higher core number densities and also reach higher densities. Despite this, the models all converge within $\approx 1 \text{ Myr}$ to a core number density of $\approx 10^5 \text{ pc}^{-3}$. The models which were initialized with lower Q also reach higher densities than their counterparts. This is expected because the colder clusters are more susceptible to the initial collapse. The increase in number of collisions for

the coldest clusters is very marginal (see Table 1) and once again, there is no increase in the fraction of VMSs that are produced.

3.2.1.2 Primordial mass segregation Many observations suggest that star clusters may form with a high degree of mass segregation (see e.g. Gouliermis et al. 2004 and Chen et al. 2007). The simulations of Moeckel & Clarke (2011) demonstrate that during the accretion phase of gas on to protostars, mass segregation naturally occurs owing to the distribution of masses of the protostars. We do not simulate this phase but, if this occurs before the stars evolve to the ZAMS, our simulations should be initialized with some degree of mass segregation. Using the algorithm of Baumgardt et al. (2008) which produces clusters in virial equilibrium for chosen degrees of mass segregation (denoted $S = 0$ for a primordially unsegregated cluster and $S = 1$ for a fully mass segregated cluster), we introduce mass segregation into the initial spherical clusters prior to scaling the axial ratios and adjusting the positions and velocities. However, the introduction of mass segregation into the models has a very minimal effect on the results of these simulations (see Table 1). The mean number of collisions remains roughly consistent with models without primordial mass segregation and there is a tendency for primordially mass segregated models to produce slightly more PISNs. The number of VMSs that form remains the same as do the average masses of the VMSs. Regardless of many assumptions made to produce the initial conditions, the masses of the VMSs are robust but f_{VMS} will change with initial central density and this is further discussed in Appendix A where we use the non-spherical initial conditions taken from the $l_{\max} = 20$ cosmological simulation to study the formation of collisional runaway in a denser cluster.

3.2.2 Spherical N -body simulations

Our simulations taking into account the flattened and asymmetric spatial distribution of the gas in the central regions of the galaxy in the cosmological hydrodynamic simulation have succeeded in producing VMSs which may directly

⁶ By “top-heavy” we mean that more mass is locked in high mass stars for this IMF compared to another we sample which has the same slope but a lower M_{\min} . This should not be confused with an IMF where most of the mass is in high mass stars.

⁷ The core radius is computed following Casertano & Hut (1985) where the density at each particle is calculated using the five nearest neighbours.

Non-Spherical Models

Initial Conditions				Results								
ρ_{init}	IMF	Q	D	S	\bar{N}_{coll}	f_{VMS}	f_{PISN}	f_{NE}	\bar{M}_{seed} M_{\odot}	$M_{\text{VMS,max}}$ M_{\odot}	\bar{M}_{VMS} M_{\odot}	M_{SMBH} $10^9 M_{\odot}$
P	TH_Salp	0.5	3.0	0.0	2.20	8.0 ± 4.0	32.0 ± 8.0	60.0 ± 11.0	83.9	323.1	297.1	2.98
P	TH_Salp	0.3	3.0	0.0	1.84	8.0 ± 4.0	40.0 ± 8.9	52.0 ± 10.2	80.9	369.9	305.3	3.06
P	TH_Salp	0.1	3.0	0.0	1.88	4.0 ± 2.8	46.0 ± 9.6	50.0 ± 10.0	82.1	303.0	297.4	2.98
P	TH_Salp	0.5	2.6	0.0	1.82	6.0 ± 3.5	24.0 ± 6.9	70.0 ± 11.8	91.0	308.6	306.5	3.08
P	TH_Salp	0.3	2.6	0.0	2.04	4.0 ± 2.8	40.0 ± 8.9	56.0 ± 10.6	89.9	336.5	309.1	3.10
P	TH_Salp	0.1	2.6	0.0	2.20	8.0 ± 4.0	38.0 ± 8.7	54.0 ± 10.4	71.6	370.5	332.5	3.34
P	TH_Salp	0.5	1.6	0.0	3.96	8.0 ± 4.0	38.0 ± 8.7	54.0 ± 10.4	82.2	398.4	302.6	3.04
P	TH_Salp	0.3	1.6	0.0	3.34	2.0 ± 2.0	52.0 ± 10.2	46.0 ± 9.6	89.2	312.6	312.6	3.14
P	TH_Salp	0.1	1.6	0.0	4.36	10.0 ± 4.5	30.0 ± 7.7	60.0 ± 11.0	73.5	356.7	316.7	3.18
P	TH_Salp	0.5	3.0	1.0	1.78	6.0 ± 3.5	32.0 ± 8.0	62.0 ± 11.1	80.1	338.8	303.6	3.05
P	TH_Salp	0.3	3.0	1.0	1.80	4.0 ± 2.8	48.0 ± 9.8	48.0 ± 9.8	82.6	300.6	287.5	2.88
P	TH_Salp	0.1	3.0	1.0	1.74	12.0 ± 4.9	30.0 ± 7.7	58.0 ± 10.8	88.2	339.7	326.0	3.27
CD	TH_Salp	0.5	3.0	0.0	1.56	6.0 ± 3.5	32.0 ± 8.0	62.0 ± 11.1	89.4	302.8	288.4	2.89
CD	TH_Salp	0.3	3.0	0.0	1.98	4.0 ± 2.8	36.0 ± 8.5	60.0 ± 11.0	74.0	275.5	268.2	2.69
CD	TH_Salp	0.1	3.0	0.0	2.06	10.0 ± 4.5	40.0 ± 8.9	50.0 ± 10.0	77.8	411.5	305.7	3.07
CD	TH_Salp	0.5	2.6	0.0	2.22	4.0 ± 2.8	38.0 ± 8.7	58.0 ± 10.8	76.1	320.5	310.0	3.11
CD	TH_Salp	0.3	2.6	0.0	1.56	0.0 ± 0.0	38.0 ± 8.7	62.0 ± 11.1	-	-	-	-
CD	TH_Salp	0.1	2.6	0.0	2.04	10.0 ± 4.5	46.0 ± 9.6	44.0 ± 9.4	86.4	332.5	302.5	3.04
CD	TH_Salp	0.5	1.6	0.0	7.90	4.0 ± 2.8	42.0 ± 9.2	54.0 ± 10.4	81.3	310.5	289.1	2.90
CD	TH_Salp	0.3	1.6	0.0	7.12	8.0 ± 4.0	36.0 ± 8.5	56.0 ± 10.6	82.7	428.6	321.1	3.22
CD	TH_Salp	0.1	1.6	0.0	8.22	2.0 ± 2.0	48.0 ± 9.8	50.0 ± 10.0	54.7	278.8	278.8	2.80
CD	TH_Salp	0.5	3.0	1.0	1.80	2.0 ± 2.0	34.0 ± 8.2	64.0 ± 11.3	99.2	358.0	358.0	3.59
CD	TH_Salp	0.3	3.0	1.0	2.20	10.0 ± 4.5	44.0 ± 9.4	46.0 ± 9.6	80.7	355.5	302.0	3.03
CD	TH_Salp	0.1	3.0	1.0	2.00	8.0 ± 4.0	48.0 ± 9.8	44.0 ± 9.4	94.9	320.2	295.4	2.96

Table 1. ρ_{init} : the initial density profile of the cluster. “P” represents a Plummer sphere and “CD” represents a constant density model. IMF: the initial stellar IMF of the models. Q : virial ratio of the initial spherical star clusters. $Q = 0.5$ represents a spherical star cluster in virial equilibrium and $Q < 0.5$ represents a dynamically colder system. D : fractal dimension of the cluster. $D = 3.0$ is a smooth cluster and $D = 1.6$ represents a very fractal distribution. S : initial degree of mass segregation in the cluster. $S = 0$ represents a cluster without mass segregation and $S = 1$ is a fully segregated cluster. \bar{N}_{coll} : average number of collisions over all of the realizations. f_{VMS} , f_{PISN} , f_{NE} : percentage of realizations which produce a VMS, PISN, or neither respectively. Error bars on these values assume Poisson statistics. \bar{M}_{seed} : average mass of the star which seeded the collisional runaway for simulations which produced a VMS. $M_{\text{VMS,max}}$: mass of the most massive VMS which formed in all of the realizations. \bar{M}_{VMS} : average mass of the VMSs which form in the simulations which produced VMSs. M_{SMBH} : the average mass of a SMBH at $z = 6$ assuming Eddington limited accretion with a radiative efficiency of $\epsilon = 0.1$. For all models, 50 realizations are simulated.

collapse into IMBHs. The simulated star clusters become spherical within a few hundred thousand years. However, note that this time-scale is dependent on the initial rotation within the sub-clumps. This has not been included in our simulations. Rotation tends to delay core collapse and should prolong the phase where the star cluster is in an asymmetric flattened state. While the clusters do become spherical rather quickly, it is important to note that the initial dynamics, in particular, differ between the non-spherical and a corresponding spherical cluster. The evolution of the core number density of a spherical model which has a similar initial central density follows closely the non-spherical models with $D = 3.0$ and $Q = 0.5$ except for an initial spike which is due to the presence of a secondary clump in the non-spherical models (see the left-hand panel of Fig. 7). This evolution differs from the colder and fractal non-spherical models in that the central number density rises slowly and does not decrease by 1 Myr. Regardless of this difference, we show in the following sections that the specific evolution makes little difference for f_{VMS} or \bar{M}_{VMS} , and the parameters that affect the results the most are the initial central density and the mass of the system. While the

change in dynamics is interesting in its own right, it appears not to be of particular importance for the results of our work here. For that reason we explore a wider range of parameters for spherical star clusters and emphasize that this is likely a safe approximation when studying parameters such as f_{VMS} or \bar{M}_{VMS} .

3.2.2.1 Setup of spherical star clusters Observations of local clusters as well as simulations (Lada & Lada 2003; Girichidis et al. 2011; Bate 2012) show that star formation occurs deeply embedded in molecular clouds and that stars tend to form in the central high-density regions. To set the radius of our spherical star clusters for a given mass, we assume an isothermal density profile. We calculate the radius of the cluster such that the mass enclosed equals $\epsilon M_{\text{clump}}$ and set this as the radius which encloses the stars up to a constant factor f_c . The mass within this radius is redistributed into a Plummer sphere and the remaining gas and dark matter are smoothed over a second Plummer sphere with a radius of the original clump multiplied by the same contraction factor f_c .

For an isothermal sphere,

$$M(r) = M_{\text{clump}} \frac{r}{R_{\text{clump}}}, \quad (4)$$

where $M_{\text{clump}} = M_* + M_g$ and R_{clump} is the initial radius of the clump. We can then calculate the stellar radius as,

$$R_* = \frac{M_* R_{\text{clump}}}{M_{\text{clump}}} = \epsilon R_{\text{clump}}, \quad (5)$$

which gives an enclosed mass profile for the stars,

$$M_*(r) = \frac{M_{*,p} r^3}{(r^2 + a_{*,p}^2)^{\frac{3}{2}}}. \quad (6)$$

Here, $M_{*,p} = [(\frac{3\pi}{16} f_c)^2 + 1]^{3/2} M_*$, $a_{*,p} = \frac{3\pi}{16} f_c R_*$ and f_c is an arbitrary contraction factor.

We set the radius of the gas, R_g , equal to the original radius of the clump times f_c , and smooth the mass over a Plummer sphere, so we find that the enclosed mass profile for the gas is,

$$M_g(r) = \frac{M_{g,p} r^3}{(r^2 + a_{g,p}^2)^{\frac{3}{2}}}, \quad (7)$$

where $M_{g,p} = [(\frac{3\pi}{16} f_c)^2 + 1]^{3/2} M_g$ and $a_{g,p} = \frac{3\pi}{16} f_c R_g$.

Fig. 4 shows that a small amount of dark matter is also present within the collapsing clump of gas at the centre of our mini-halo. We include this mass in the external gas potential of our star cluster

In Fig. 8, we plot the average initial density profiles for spherical clusters with $f_c = 0.1, 0.2, 0.3$, and 0.5 and compare with the spherically averaged density profiles of the Plummer and constant density models for our non-spherical star clusters discussed in Section 3.2.1. Note that the Plummer models used in the non-spherical simulations are similar to the models used in the spherical simulations with $f_c = 0.5$. The constant-density models used in the non-spherical simulations are less dense in the inner regions than all of the spherical models considered here; however, they maintain a higher density at larger radii. We found, however, that the difference between the Plummer and constant-density models does not significantly affect the probabilities of forming a VMS nor how massive these stars become. For this reason, we only investigate spherical clusters with Plummer density profiles.

3.2.2.2 Varying f_c , Q , and D In Table 2, we list the initial conditions for these spherical models where we vary f_c , Q , and D . As we have seen in Fig. 8, f_c controls the initial central density of the cluster and we found that for fixed mass, the initial central density is the most important parameter in determining what percentage of clusters produce a VMS as well as how massive the VMS can grow (see Table 2). In Fig. 9, we plot the mass of the most massive VMS that formed as well as the fraction of clusters which produced a VMS as a function of initial central density. Both the fraction and the mass of the VMS are increasing with the increase in initial central density. The increase of both of these values is reasonably linear in $\log \rho$ and can be approximated as

$$f_{\text{VMS}} = 42.6 \log_{10}(\rho_{*,\text{max}}) - 231.2 \text{ per cent}, \quad (8)$$

and

$$M_{\text{VMS,max}} = 214.1 \log_{10}(\rho_{*,\text{max}}) - 900.1 M_{\odot}. \quad (9)$$

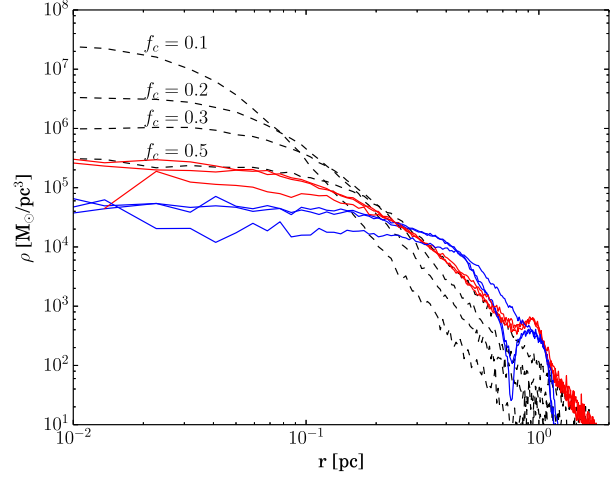


Figure 8. Density profiles of spherical models (dashed black) are compared with the spherically averaged density profiles of the non-spherical models. The red line indicates models with a Plummer density profile and the blue line is for models with a constant density profile and the three different lines show $D = 3.0, 2.6$, and 1.6 . The models with $D = 3.0$ and 2.6 are indistinguishable while the models with $D = 1.6$ have a slightly lower density in the inner regions of the cluster. Spherical models with decreasing central densities represent clusters with $f_c = 0.1, 0.2, 0.3$, and 0.5 as annotated. f_c is the fraction by which the initial radius of the clump is contracted to produce these models.

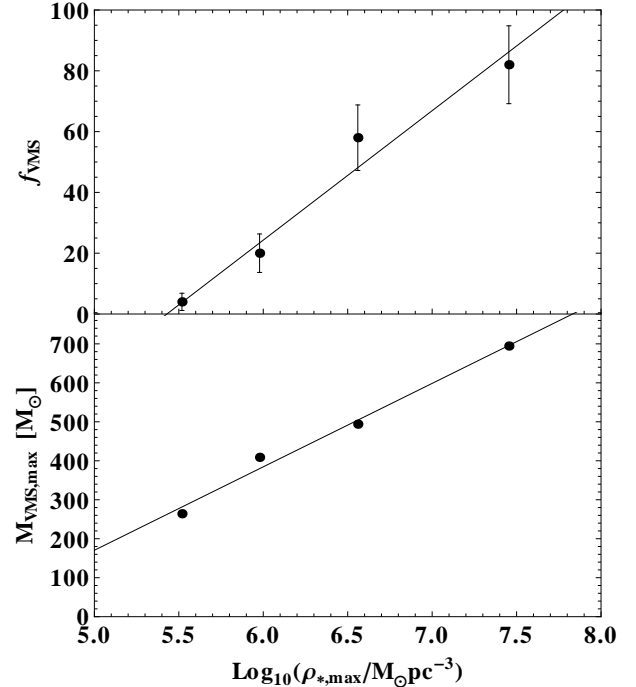


Figure 9. f_{VMS} (top) and $M_{\text{VMS,max}}$ (bottom) as a function of the initial central stellar mass density for the TH_Salp IMF assuming $S = 0$ and $b = 0$. The data points come directly from the simulations and error bars are 1σ Poisson errors. We over plot the best fit lines from equations (8) & (9).

Spherical Models

Initial Conditions				Results							
$R_{*,vir}$ pc	f_c	Q	D	\bar{N}_{coll}	f_{VMS} per cent	f_{PISN} per cent	f_{NE} per cent	\bar{M}_{seed} M_\odot	$M_{VMS,max}$ M_\odot	\bar{M}_{VMS} M_\odot	M_{SMBH} $10^9 M_\odot$
0.071	0.1	0.5	3.0	9.08	82.0 ± 12.8	18.0 ± 6.0	0.0 ± 0.0	83.9	694.5	477.9	4.80
0.143	0.2	0.5	3.0	4.56	58.0 ± 10.8	30.0 ± 7.7	12.0 ± 4.9	86.6	494.0	355.6	3.57
0.215	0.3	0.5	3.0	2.48	20.0 ± 6.3	55.0 ± 10.5	24.0 ± 6.9	86.3	408.8	336.5	3.38
0.358	0.5	0.5	3.0	1.12	4.0 ± 2.8	38.0 ± 8.7	58.0 ± 10.8	85.3	264.1	263.6	2.65
0.358	0.5	0.5	2.6	1.48	4.0 ± 2.8	44.0 ± 9.4	52.0 ± 10.2	92.4	382.4	338.2	3.39
0.358	0.5	0.5	1.6	3.28	4.0 ± 2.8	50.0 ± 10.0	46.0 ± 9.6	78.5	301.0	297.0	2.98
0.358	0.5	0.3	3.0	0.92	0.0 ± 0.0	40.0 ± 8.9	60.0 ± 11.0	-	-	-	-
0.358	0.5	0.3	2.6	1.28	0.0 ± 0.0	52.0 ± 10.2	48.0 ± 9.9	-	-	-	-
0.358	0.5	0.3	1.6	3.02	6.0 ± 3.5	38.0 ± 8.7	56.0 ± 10.6	84.6	303.1	326.3	3.27

Table 2. All models assume a TH_Salp IMF with $M_{min} = 1 M_\odot$, $M_{max} = 100 M_\odot$, $\epsilon = 2/3$, and $M_* = 1.01 \times 10^4 M_\odot$. $R_{*,vir}$: virial radius of the stellar component. f_c : contraction factor. For all models, 50 realizations are used. See Table 1 for definitions of other values.

Initial Mass Functions			
Name	M_{min} M_\odot	M_{max} M_\odot	α
Salp	0.1	100.0	-2.35
TH_Salp	1.0	100.0	-2.35
Kroupa	0.1	0.5	-1.3
	0.5	100.0	-2.30
Flat	1.0	100.0	-2.00

Table 3. Table of the different IMFs sampled for the simulations of spherical star clusters.

Decreasing Q from 0.5 to 0.3 does not affect f_{VMS} or \bar{N}_{coll} , similarly to the non-spherical models. We found a small increase in \bar{N}_{coll} for the more inhomogeneous models similar to what we found for our non-spherical NBODY6 simulations. This is likely to be due to the higher local initial densities. The value of D , however, does not change f_{VMS} . Based on the results in Table 2, a spherical cluster with f_c between 0.5 and 0.3, $Q = 0.5$ and $D = 3.0$ should give very similar results to the non-spherical models.

3.2.2.3 Varying the IMF As the stellar IMF is highly uncertain, especially at high redshift, we test the effect of varying the IMF. The parameters of the different IMFs implemented are listed in Table 3. In Table 4, we list the initial conditions and results of the models where the IMF is varied. For these models, we have assumed $f_c = 0.2$ which was previously determined to have a high percentage of models which produce a VMS (see Table 2).

As the mean mass of the IMF is increased, the fraction of realizations which produce a VMS remain consistent within error bars and therefore, regardless of the IMF, the likelihood of producing a VMS in a high-redshift NSC is the same for an NSC of this mass. The average number of stellar collisions increases, however, for models with lower average stellar mass (\bar{m}) due to the higher number density of stars. Furthermore, $M_{VMS,max}$ and \bar{M}_{seed} tend to increase as the IMF becomes more top heavy. This is expected because there are simply more high-mass stars in the runs with more top-heavy IMFs and therefore the mean mass per collision

will increase. We can also see that \bar{M}_{seed} slightly increases with increasing \bar{m} which also reflects the availability of more high-mass stars.

3.2.2.4 Primordial binaries and mass segregation:

Observations suggest the presence of a significant fraction of binaries in young stellar clusters, especially for high-mass stars (Hut et al. 1992; Sana et al. 2009). A large binary fraction at the centres of star clusters can effectively heat the cluster and prevent core collapse. This decreases the maximum value of the central density which may inhibit the formation of a VMS due to collisional runaway. When clusters are initialized with binaries, massive stars with mass greater than $5 M_\odot$ are preferentially put in binaries. For low-mass binaries, we use a period distribution consistent with Kroupa (1995) and for binary stars which have a primary star with mass greater than $5 M_\odot$, we adopt the period distribution consistent with Sana & Evans (2011). We test the effects of including primordial binaries as well as primordial mass segregation for these spherical clusters and list the initial conditions in Table 5.

Introducing mass segregation for models with TH_Salp and Kroupa IMFs makes no difference to \bar{M}_{VMS} . The same is true when binaries are introduced. In all cases, the average VMS undergoes $\approx 1 - 3$ collisions after the PISN mass threshold and with these low number statistics, it is unsurprising that \bar{M}_{VMS} is roughly the same regardless of variations to these initial parameters. We do, however, see a drastic increase in \bar{N}_{coll} when the clusters are initialized with large binary fractions. The increase of the total number of collisions in the cluster is clearly not affecting \bar{M}_{VMS} . For stars that are in binaries from the beginning, interactions with other stars can efficiently remove energy from the binary and eventually drive the binary to a merger. Without binaries, the massive stars first have to sink to the centre of the cluster and dynamically form binaries before merging can take place. The average mass of the mergers is, however, much lower for simulations with primordial binaries and these newly formed, merged stars tend to have very little impact on the formation of a VMS. Despite the evolution of the star cluster being significantly different for simulations with primordial mass segregation and binaries, we can make

Spherical Models: Varying the Stellar IMF

Initial Conditions			Results							
IMF	\bar{M}_{\max} M_{\odot}	\bar{m} M_{\odot}	\bar{N}_{coll}	f_{VMS} per cent	f_{PISN} per cent	f_{NE} per cent	\bar{M}_{seed} M_{\odot}	$M_{\text{VMS,max}}$ M_{\odot}	\bar{M}_{VMS} M_{\odot}	M_{SMBH} $10^9 M_{\odot}$
Salp	79.5	0.35	8.95	40.0 ± 14.1	50.0 ± 15.8	10.0 ± 7.1	75.2	353.1	295.3	2.96
TH_Salp	90.4	3.09	4.56	58.0 ± 10.8	30.0 ± 7.7	12.0 ± 4.9	86.6	494.0	355.6	3.57
Kroupa	88.8	0.64	5.80	44.0 ± 9.4	38.0 ± 8.7	18.0 ± 6.0	84.0	433.2	333.9	3.35
Flat	96.1	4.65	3.44	48.0 ± 9.8	40.0 ± 8.9	12.0 ± 4.9	89.9	591.5	376.7	3.78

Table 4. \bar{M}_{\max} : the average maximum mass star over all realizations of the cluster. \bar{m} : the average stellar mass over all realizations of the cluster. See Table 1 for definitions of other values. 50 realizations were run for all models except the model with the Salp IMF where only 20 simulations are used.

Spherical Models: Primordial Binaries and Mass Segregation

Initial Conditions					Results							
IMF	\bar{M}_{\max} M_{\odot}	\bar{m} M_{\odot}	S	b	\bar{N}_{coll}	f_{VMS} per cent	f_{PISN} per cent	f_{NE} per cent	\bar{M}_{seed} M_{\odot}	$M_{\text{VMS,max}}$ M_{\odot}	\bar{M}_{VMS} M_{\odot}	M_{SMBH} $10^9 M_{\odot}$
TH_Salp	90.4	3.09	0.0	0.0	4.56	58.0 ± 10.8	30.0 ± 7.7	12.0 ± 4.9	86.6	494.0	355.6	3.57
TH_Salp	90.4	3.11	0.5	0.0	4.78	66.0 ± 11.4	26.0 ± 7.2	8.0 ± 4.0	85.8	516.8	352.7	3.54
TH_Salp	90.6	3.08	1.0	0.0	3.64	36.0 ± 8.5	48.0 ± 9.8	16.0 ± 5.7	83.2	406.1	318.5	3.20
TH_Salp	92.6	3.10	0.0	0.5	17.6	32.0 ± 8.0	50.0 ± 10.0	18.0 ± 6.0	81.9	438.4	319.0	3.20
TH_Salp	91.5	3.09	0.0	1.0	22.0	22.0 ± 6.6	50.0 ± 10.0	28.0 ± 7.5	79.0	445.0	327.0	3.28
TH_Salp	91.4	3.09	0.5	0.5	18.0	42.0 ± 9.2	44.0 ± 9.4	14.0 ± 5.3	81.5	515.1	344.0	3.45
TH_Salp	90.6	3.09	1.0	0.5	16.8	24.0 ± 6.9	36.0 ± 8.5	40.0 ± 8.9	83.2	477.7	336.7	3.38
TH_Salp	90.0	3.09	0.5	1.0	23.7	46.0 ± 9.6	36.0 ± 8.5	18.0 ± 6.0	80.1	465.3	353.7	3.55
TH_Salp	91.2	3.08	1.0	1.0	22.7	26.0 ± 7.2	38.0 ± 8.7	26.0 ± 7.2	82.2	595.6	365.9	3.67
Kroupa	88.8	0.64	0.0	0.0	5.80	44.0 ± 9.4	38.0 ± 8.7	18.0 ± 6.0	84.0	433.2	333.9	3.35
Kroupa	87.2	0.64	0.5	0.0	6.18	42.0 ± 9.2	50.0 ± 10.0	8.0 ± 4.0	80.0	410.7	336.6	3.38
Kroupa	85.8	0.64	1.0	0.0	5.24	52.0 ± 10.2	38.0 ± 8.7	10.0 ± 4.5	78.9	435.5	327.7	3.29

Table 5. Note that the TH_Salp and Kroupa models with $S = 0$ and $b = 0$ are the same models listed in Table 4 and are shown here for ease of comparison. See Table 1 for definitions of values. For all models, 50 realizations are run.

robust predictions for the average mass of a VMS that will form.

Although \bar{M}_{VMS} is only weakly dependent on most assumptions we have made, we do find a factor of 3 change in the fraction of models which produce a VMS when including mass segregation and binaries. While this does not affect the mass function of these objects, it does affect their number density. Introducing binaries tends to decrease the number of VMSs which form while no trend is evident for increasing the primordial mass segregation. Including the binaries tends to heat the core and eject the low-mass stars, and this influences the evolution of the core of the cluster where the collisions occur. The effect of changing these assumptions is, however, much less significant than changes to the central mass density of the star cluster.

3.2.2.5 Varying the mass of the NSC Thus far, our work has focused on one simulation of one mini-halo with one NSC with a particular mass motivated by our cosmological zoom-in simulation. The Universe likely exhibits a range of NSC masses with varying initial central densities and we also want to explore how our results depend on the assumed mass of the NSC. Although the first collapsing halo in our simulation is not be metal enriched, to get an idea of the variance in the mass of the NSCs in the early Universe, we can apply the same criteria that we used to define the NSC

in the secondary collapsing halo to determine an NSC mass for the first halo. The total mass of the NSC in this halo including gas and dark matter is $\approx 2.3 \times 10^4 M_{\odot}$, which is clearly more massive than the NSC in the secondary collapsing object. We run a few additional simulations where we multiply the total mass of the spherical $f_c = 0.2$ model by some factor f_m and correspondingly increase the radius of this model by $f_m^{1/3}$ in order to determine how massive an IMBH may become for different NSC masses. In Table 6, we list the initial conditions and results of these models which have been averaged over 25 realizations. For all models, we assume a TH_Salp IMF and Plummer model initial conditions⁸.

It is clear that for these more massive NSCs, the majority are likely to form an IMBH with some producing IMBHs with masses greater than $1000 M_{\odot}$. The average masses of the VMS are also significantly higher.

3.3 Caveats and Limitations

The initial conditions of our models, in particular the central number and mass densities, play a major role in determining the fraction of clusters which produce a VMS. Owing

⁸ Note that models with larger f_m maintain a higher average density at larger radii.

Spherical Models: Varying the Mass of the NSC

Initial Conditions					Results							
f_m	\bar{M}_{\max} M_{\odot}	\bar{m} M_{\odot}	S	b	\bar{N}_{coll}	f_{VMS} per cent	f_{PISN} per cent	f_{NE} per cent	\bar{M}_{seed} M_{\odot}	$M_{\text{VMS,max}}$ M_{\odot}	\bar{M}_{VMS} M_{\odot}	M_{SMBH} $10^9 M_{\odot}$
2	94.8	3.09	0.0	0.0	7.20	80.0 ± 17.9	20.0 ± 8.9	0.00 ± 0.0	89.1	875.8	495.2	4.97
3	96.7	3.09	0.0	0.0	9.48	96.0 ± 19.6	4.0 ± 4.0	0.00 ± 0.0	87.3	860.9	611.1	6.13
4	97.2	3.09	0.0	0.0	11.36	96.0 ± 19.6	4.0 ± 4.0	0.00 ± 0.0	88.2	1016.7	671.4	6.74

Table 6. f_m : fraction by which the mass of the NSC is scaled. The radius is scaled by $f_m^{1/3}$. See Table 1 for definitions of other values.

to numerical limitations, to the best of our knowledge, there is no study to date which has produced an embedded cluster such as the one presented in this paper that had an IMF consistent with observations which has been evolved from the protostellar accretion phase all the way to the onset of the ZAMS. There is thus a clear disconnect between the types of simulations which can form protostellar cores directly from molecular clouds and the direct N-body simulations which can follow the subsequent evolution of these stars once the cluster has completely formed. Simulations which follow the initial formation and gas accretion on to protostellar cores explore how the physical properties of the collapsing molecular cloud and the accretion dynamics affect the initial conditions of the star cluster (Bate 1998; Bate & Bonnell 2005; Bate 2012; Krumholz et al. 2012). We are unable to capture this direct link between the properties of the birth cloud and the initial conditions of the star cluster with our direct N-body calculations. In order to properly model this system, we would have to self-consistently predict the distribution function and IMF of stars from the cosmological simulation and run the simulation far beyond the initial stages of collapse. This is, unfortunately, beyond current numerical capabilities. We have, however, mitigated this by studying a large number of possible initial conditions for the star clusters we have simulated. We believe that we can therefore confidently conclude that for our choice of physically motivated and reasonable assumptions, our simulations predict collisional runaway to be a promising mechanism for the formation of VMSs.

We have allowed the stars to grow far beyond the masses at which stellar evolution is well understood due to the lack of observational constraints. In this regime, it is not obvious whether such an object is stable and evolves like a normal star especially because it is created by merging. For low-metallicity stars, the main-sequence lifetime and radius, which are the most important stellar parameters for this work, begin to flatten at high masses. For these reasons, we have chosen to evolve them as $100 M_{\odot}$ stars. Two other processes along these lines are neglected in our simulations that will affect stellar collisions, the inflation of the collisional remnant's radius and the possible increase in the remnant's main-sequence lifetime. When stars undergo collisions, some of the kinetic energy from the collision is absorbed into the envelope of the primary which can cause the merger remnant to have a much greater radius than a comparable star with that mass which evolves normally on the main sequence (Dale & Davies 2006). The lifetime of this stage is likely much shorter than the main-sequence lifetime of the star. However, the gravitationally focusing

cross-section of the star scales with radius so the probability of undergoing a collision can greatly increase during this period (Dale & Davies 2006). Further collisions will cause a similar effect, and thus, if the time between collisions is short, the inflated radius can be sustained for long periods of time. The mixing of the two colliding stars can introduce a fresh source of hydrogen into the core and can increase the main-sequence lifetime of the remnant compared to a star with a similar mass that evolves normally on the main sequence (Glebbeek et al. 2008, 2013). The prolonged lifetime will increase the number of stellar collisions that remnant might undergo. Both effects tend to improve the prospect of forming a VMS and by neglecting them, our results should be conservative in this regard.

4 IMPLICATIONS FOR THE (EARLY) GROWTH OF SUPERMASSIVE BLACK HOLES

We have demonstrated that high-redshift, dense, metal-poor NSCs are likely to host runaway stellar collisions which produce VMSs and that this process is robust to a wide variety of assumptions. We have, however, not addressed here what happens to the VMS once it forms and there are also no observational constraints for stars of this mass. Heger et al. (2003) predict that VMSs with the mass and metallicity as in our work end their lives by directly collapsing into an IMBH with minimal mass-loss. However, these predictions need probably to be considered with a healthy scepticism given the lack of observational constraints. Furthermore, we have assumed that when the stars merge, the remnant becomes an ordinary main-sequence star. This is also uncertain as the impact of the merge certainly disrupts the star at least temporarily and the subsequent stellar evolution also remains uncertain. With these caveats in mind, we now assess briefly whether this mechanism can be responsible for producing the population of bright quasars at $z \approx 6 - 7$ which has an observed lower limit of $1.1 \times 10^{-9} \text{ Mpc}^{-3}$ (Venemans et al. 2013). To do this, we estimate the mass to which IMBHs can grow by these lower redshifts and their expected space density.

Under the assumption of Eddington-limited accretion, the mass of a black hole increases as $M = M_0 e^{((1-\epsilon)/\epsilon)(t/t_{\text{Edd}})}$ where ϵ is the radiative efficiency and $t_{\text{Edd}} = \sigma_T c / (4\pi G m_p)$ (Frank et al. 2002). The size of ϵ is somewhat uncertain and depends on the properties of the accretion disc which surrounds the black hole as well as the spin of the black hole. Our direct N-body simulations are run for 3.5 Myr after the point at which we extract the clump

from the simulation. This corresponds to the lifetimes of the most massive stars. By this point, the hydrodynamic simulation would have evolved to $z = 25.88$. Assuming a canonical value of $\epsilon = 0.1$ we calculate the expected mass of the black hole at $z = 6$ and tabulate the results in Tables 1, 2, 4, 5, and 6. It is clear that regardless of many of the initial assumptions of the IMF, binary fraction, initial mass segregation, SFE, and density profile, the average masses of the VMSs that do form are sufficient to grow to the masses of the black holes powering high-redshift quasars that we observe at $z \gtrsim 6$ if the black holes can be continuously fed at the Eddington accretion rate.

The mass range that we predict for our VMSs is well within the range predicted by some simulations of Pop. III stars (Hirano et al. 2014). For simple models assuming Eddington-limited accretion, there is thus little difference between assuming that the growth of SMBHs starts with the remnants of Pop. III stars and assuming that the growth is seeded by the VMS resulting from runaway growth in Pop. II star cluster. What makes the latter route perhaps more promising is, however, the very different environment in which the collisional runaway VMSs form compared to that of Pop. III stars. Johnson & Bromm (2007) predict a long time delay for efficient accretion on to a black hole in the mass range studied in this work due to radiative feedback on the surrounding medium. Only in haloes where the gas density remains sufficiently high can this be avoided although even if the gas remains at high densities, the radiative feedback still may limit the accretion to sub-Eddington levels (Milosavljević et al. 2009). Mergers with surrounding mini-haloes may provide the dense gas supply necessary to overcome most of the radiative feedback and efficiently feed the black hole. Recall that the formation of a Pop. II NSC at these very high redshifts we study requires a close neighbouring halo which can pollute the halo in which the IMBH forms with metals. The haloes in our hydrodynamic simulations merge shortly after the IMBH is likely to form. Thus, it appears unlikely that an IMBH which may form in our simulations would suffer a long period of inefficient accretion.

A further difference between a Pop. III remnant black hole and the IMBHs forming from runaway stellar collisions is the presence of a surrounding star cluster in the latter scenario. Alexander & Natarajan (2014) discuss the evolution of low-mass black holes with $\approx 10 M_\odot$ embedded in a star cluster fed by dense gas flows and accreting at super-Eddington rates due to random motions within the cluster. If high-redshift, dense star clusters have very top-heavy IMFs, this may indeed be relevant for more massive black hole seeds. A similar mechanism was indeed suggested by Davies et al. (2011) where dense inflows of gas can initiate core collapse and cause efficient merging in the central regions of the cluster. The presence of the cluster after the seed has formed may be key to allowing it to grow efficiently.

Assuming that these SMBH seeds can accrete at the required rates, we can calculate an approximate upper limit on the number density of SMBHs by calculating the total number density of haloes enriched above the critical metallicity at the final redshift, z_{fin} , such that IMBHs can grow to $10^9 M_\odot$ by $z = 6$. Assuming that the average mass of an IMBH that forms in our simulation is $300 M_\odot$, $z_{fin} = 20$. The number density of SMBHs at $z = 6$ then is approxi-

mately

$$n_{\text{SMBH}} = f_p f_f f_{\text{edd}} n_{\text{gal}}(> M_{\text{thresh}}), \quad (10)$$

where f_p is the fraction of haloes at z_{fin} that have been metal enriched above Z_{crit} , f_f is the fraction of these haloes that form an IMBH, f_{edd} is the fraction of the black holes which can sustain Eddington-limited accretion, and $n_{\text{gal}}(> M_{\text{thresh}})$ is the total number density of galaxies above the mass threshold, M_{thresh} , which are possible sites for forming an IMBH. We set $M_{\text{thresh}} = 5 \times 10^6 M_\odot$, and using the Jenkins mass function (Jenkins et al. 2001), we find, $n_{\text{gal}} \approx 8 \text{ Mpc}^{-3}$. For the mass of the NSC which formed in our simulation, f_f is likely < 0.1 . There is little constraint on the value of f_p as we have little knowledge of the metal enrichment of the intergalactic medium at these extremely high redshifts. Metal enrichment in the early Universe is almost certainly very patchy and confined to overdense regions. However, even for $f_f = 0.01$, a rather small value of $f_p \approx 10^{-5}$ would be sufficient to explain the observed SMBH number density based on this simple estimate with $f_{\text{edd}} = 1$. The value of f_{edd} also remains highly uncertain and it is unlikely to be unity given the plethora of environmental feedback mechanisms that inhibit efficient accretion on to black holes (Johnson & Bromm 2007; Milosavljević et al. 2009; Park & Ricotti 2011). For this to occur, black holes would require a constant supply of cold, low-angular-momentum gas, and since we do not follow the hydrodynamical simulation past the formation of the NSC birth cloud, it is uncertain whether such a reservoir is available. Note, however, that the mass function of IMBHs forming in high-redshift NSCs is unlikely to be a delta function at the minimum mass required to form an SMBH by $z = 6$ so f_{edd} need not be 1 for this process to produce the population of observed SMBHs at $z = 6$. In addition, other mechanisms may allow black holes to accrete at super-Eddington rates when a surrounding star cluster is present (Davies et al. 2011; Alexander & Natarajan 2014).

5 CONCLUSIONS

Using a combination of high-resolution, hydrodynamic cosmological zoom-in simulations and spherical and non-spherical direct N-body simulations, we have demonstrated that stellar runaway growth at the centre of nuclear Pop. II star clusters in high-redshift protogalaxies ($20 \lesssim z \lesssim 30$) metal enriched by nearby companions is a promising route to form VMSs with masses as high as $300 - 1000 M_\odot$. We find that the average masses of the VMSs that are produced in NSCs with an expected total mass of typically $M_* \approx 10^4 M_\odot$ are relatively robust to changes in the stellar IMF, number of primordial binaries, initial degree of mass segregation, as well as initial density profile, but increase strongly with the increase in initial central density and total mass of the star cluster. If the VMSs formed in this way can directly collapse to IMBHs with moderate mass-loss, they are promising seeds for growth into the billion solar-mass black holes observed at $z \approx 6$. Our simulations further predict an enhanced number of PISNs as the simulations which fail to produce a VMS often host at least one or two high-mass collisions. This may result in a rapid early enrichment of the IGM with metals and may cause the early pollution of

other protogalaxies making them also susceptible to the collisional runaway process. Modelling the evolution of the host galaxy post-supernova will be needed to predict the effects of these PISNs on their environment

The presence of a large numbers of accreting IMBHs as well as an enhanced rate of PISN should significantly alter the early evolution of galaxies and will have important implications for the interpretation of observations of the high-redshift Universe.

ACKNOWLEDGEMENTS

We thank the referee for their comments and revisions. HK is grateful to Sverre Aarseth and Simon Karl for useful discussions about NBODY6 and very much appreciates the hospitality of the Foundation Boustany during his stay in Monaco where parts of this manuscript were written. We also thank John Regan, Chris Tout, and Sverre Aarseth for comments which greatly improved the manuscript. This work made considerable use of the open source analysis software PYNBODY (Pontzen et al. 2013). HK's work is partially supported by Foundation Boustany, Cambridge Overseas Trust, and an Isaac Newton Studentship. Support by ERC Advanced Grant 320596 'The Emergence of Structure during the Epoch of Reionization' is gratefully acknowledged.

This work was performed using the DiRAC/Darwin Supercomputer hosted by the University of Cambridge High Performance Computing Service (<http://www.hpc.cam.ac.uk/>), provided by Dell Inc. using Strategic Research Infrastructure Funding from the Higher Education Funding Council for England and funding from the Science and Technology Facilities Council. Cosmological hydrodynamic simulations were performed on the DARWIN cluster while all direct N -body runs were performed on the WILKES

Furthermore, this work used the DiRAC Complexity system, operated by the University of Leicester IT Services, which forms part of the STFC DiRAC HPC Facility (www.dirac.ac.uk). This equipment is funded by BIS National E-Infrastructure capital grant ST/K000373/1 and STFC DiRAC Operations grant ST/K0003259/1. DiRAC is part of the National E-Infrastructure.

REFERENCES

- Aarseth S. J., 1999, *PASP*, 111, 1333
 Alexander T., Natarajan P., 2014, *Science*, 345, 1330
 Aykutalp A., Wise J. H., Spaans M., Meijerink R., 2014, *ArXiv e-prints*
 Baraffe I., Heger A., Woosley S. E., 2001, *ApJ*, 550, 890
 Bate M. R., 1998, *ApJ*, 508, L95
 Bate M. R., 2012, *MNRAS*, 419, 3115
 Bate M. R., Bonnell I. A., 2005, *MNRAS*, 356, 1201
 Baumgardt H., De Marchi G., Kroupa P., 2008, *ApJ*, 685, 247
 Begelman M. C., Rees M. J., 1978, *MNRAS*, 185, 847
 Begelman M. C., Volonteri M., Rees M. J., 2006, *MNRAS*, 370, 289
 Behroozi P. S., Wechsler R. H., Wu H.-Y., 2013, *ApJ*, 762, 109
 Bleuler A., Teyssier R., 2014, *ArXiv e-prints*
 Bromm V., Coppi P. S., Larson R. B., 2002, *ApJ*, 564, 23
 Casertano S., Hut P., 1985, *ApJ*, 298, 80
 Ceverino D., Dekel A., Bournaud F., 2010, *MNRAS*, 404, 2151
 Chen L., de Grijs R., Zhao J. L., 2007, *AJ*, 134, 1368
 Choi J.-H., Shlosman I., Begelman M. C., 2013, *ApJ*, 774, 149
 Costa T., Sijacki D., Trenti M., Haehnelt M. G., 2014, *MNRAS*, 439, 2146
 Dale J. E., Davies M. B., 2006, *MNRAS*, 366, 1424
 Davies M. B., Miller M. C., Bellovary J. M., 2011, *ApJ*, 740, L42
 Devecchi B., Volonteri M., 2009, *ApJ*, 694, 302
 Dib S., Piau L., Mohanty S., Braine J., 2011, *MNRAS*, 415, 3439
 Eisenstein D. J., Loeb A., 1995, *ApJ*, 443, 11
 Espinoza P., Selman F. J., Melnick J., 2009, *A&A*, 501, 563
 Federrath C., Sur S., Schleicher D. R. G., Banerjee R., Klessen R. S., 2011, *ApJ*, 731, 62
 Frank J., King A., Raine D. J., 2002, *Accretion Power in Astrophysics: Third Edition*
 Freitag M., Gürkan M. A., Rasio F. A., 2006, *MNRAS*, 368, 141
 Fujii M. S., 2014, *ArXiv e-prints*
 Girichidis P., Federrath C., Banerjee R., Klessen R. S., 2011, *MNRAS*, 413, 2741
 Glebbeek E., Gaburov E., de Mink S. E., Pols O. R., Portegies Zwart S. F., 2009, *AAP*, 497, 255
 Glebbeek E., Gaburov E., Portegies Zwart S., Pols O. R., 2013, *MNRAS*, 434, 3497
 Glebbeek E., Pols O. R., Hurley J. R., 2008, *AAP*, 488, 1007
 Goodwin S. P., Whitworth A. P., 2004, *A&A*, 413, 929
 Gouliermis D., Keller S. C., Kontizas M., Kontizas E., Bellas-Velidis I., 2004, *A&A*, 416, 137
 Grassi T., Bovino S., Schleicher D. R. G., Prieto J., Seifried D., Simoncini E., Gianturco F. A., 2014, *MNRAS*, 439, 2386
 Greif T. H., Springel V., White S. D. M., Glover S. C. O., Clark P. C., Smith R. J., Klessen R. S., Bromm V., 2011, *ApJ*, 737, 75
 Hahn O., Abel T., 2011, *MNRAS*, 415, 2101
 Haiman Z., 2006, *NewArticles*, 50, 672
 Heger A., Fryer C. L., Woosley S. E., Langer N., Hartmann D. H., 2003, *ApJ*, 591, 288
 Hirano S., Hosokawa T., Yoshida N., Umeda H., Omukai K., Chiaki G., Yorke H. W., 2014, *ApJ*, 781, 60
 Hosokawa T., Omukai K., Yoshida N., Yorke H. W., 2011, *Science*, 334, 1250
 Hurley J. R., Pols O. R., Tout C. A., 2000, *MNRAS*, 315, 543
 Hurley J. R., Tout C. A., Pols O. R., 2002, *MNRAS*, 329, 897
 Hut P. et al., 1992, *PASP*, 104, 981
 Inayoshi K., Omukai K., 2011, *MNRAS*, 416, 2748
 Inayoshi K., Tanaka T. L., 2014, *ArXiv e-prints*
 Jenkins A., Frenk C. S., White S. D. M., Colberg J. M., Cole S., Evrard A. E., Couchman H. M. P., Yoshida N., 2001, *MNRAS*, 321, 372
 Johnson J. L., Bromm V., 2007, *MNRAS*, 374, 1557
 Kroupa P., 1995, *MNRAS*, 277, 1507

- Krumholz M. R., Klein R. I., McKee C. F., 2012, *ApJ*, 754, 71
- Küpper A. H. W., Maschberger T., Kroupa P., Baumgardt H., 2011, *MNRAS*, 417, 2300
- Lada C. J., Lada E. A., 2003, *ARAA*, 41, 57
- Lada C. J., Lombardi M., Alves J. F., 2010, *ApJ*, 724, 687
- Latif M. A., Bovino S., Grassi T., Schleicher D. R. G., Spaans M., 2014a, *ArXiv e-prints*
- Latif M. A., Bovino S., Van Borm C., Grassi T., Schleicher D. R. G., Spaans M., 2014b, *MNRAS*, 443, 1979
- Latif M. A., Schleicher D. R. G., Bovino S., Grassi T., Spaans M., 2014c, *ApJ*, 792, 78
- Leitherer C. et al., 1999, *ApJS*, 123, 3
- Lewis A., Challinor A., Lasenby A., 2000, *ApJ*, 538, 473
- Lodato G., Natarajan P., 2006, *MNRAS*, 371, 1813
- Loeb A., Rasio F. A., 1994, *ApJ*, 432, 52
- Milosavljević M., Couch S. M., Bromm V., 2009, *ApJ*, 696, L146
- Moeckel N., Clarke C. J., 2011, *MNRAS*, 410, 2799
- Nitadori K., Aarseth S. J., 2012, *MNRAS*, 424, 545
- Omukai K., Schneider R., Haiman Z., 2008, *ApJ*, 686, 801
- Park K., Ricotti M., 2011, *ApJ*, 739, 2
- Pfalzner S., Kaczmarek T., 2013, *A&A*, 559, A38
- Planck Collaboration et al., 2013, *ArXiv e-prints*
- Plummer H. C., 1911, *MNRAS*, 71, 460
- Pontzen A., Roškar R., Stinson G. S., Woods R., Reed D. M., Coles J., Quinn T. R., 2013, *pynbody: Astrophysics Simulation Analysis for Python. Astrophysics Source Code Library*, ascl:1305.002
- Portegies Zwart S. F., Baumgardt H., Hut P., Makino J., McMillan S. L. W., 2004, *Nature*, 428, 724
- Prieto J., Jimenez R., Haiman Z., 2013, *MNRAS*, 436, 2301
- Regan J. A., Haehnelt M. G., 2009, *MNRAS*, 396, 343
- Regan J. A., Johansson P. H., Haehnelt M. G., 2014a, *MNRAS*, 439, 1160
- Regan J. A., Johansson P. H., Wise J. H., 2014b, *ArXiv e-prints*
- Ritter J. S., Safranek-Shrader C., Gnat O., Milosavljević M., Bromm V., 2012, *ApJ*, 761, 56
- Robertson B. E., Kravtsov A. V., 2008, *ApJ*, 680, 1083
- Safranek-Shrader C., Milosavljević M., Bromm V., 2014, *MNRAS*, 440, L76
- Sana H., Evans C. J., 2011, in *IAU Symposium*, Vol. 272, IAU Symposium, Neiner C., Wade G., Meynet G., Peters G., eds., pp. 474–485
- Sana H., Gosset E., Evans C. J., 2009, *MNRAS*, 400, 1479
- Schaerer D., 2002, *A&A*, 382, 28
- Schneider R., Omukai K., Bianchi S., Valiante R., 2012, *MNRAS*, 419, 1566
- Shang C., Bryan G. L., Haiman Z., 2010, *MNRAS*, 402, 1249
- Sijacki D., Springel V., Haehnelt M. G., 2009, *MNRAS*, 400, 100
- Sugimura K., Omukai K., Inoue A. K., 2014, *MNRAS*, 445, 544
- Teyssier R., 2002, *AAP*, 385, 337
- Tout C. A., Aarseth S. J., Pols O. R., Eggleton P. P., 1997, *MNRAS*, 291, 732
- Trac H., Sills A., Pen U.-L., 2007, *MNRAS*, 377, 997
- Truelove J. K., Klein R. I., McKee C. F., Holliman, II J. H., Howell L. H., Greenough J. A., 1997, *ApJL*, 489, L179
- Turk M. J., Oishi J. S., Abel T., Bryan G. L., 2012, *ApJ*, 745, 154
- Šubr L., Kroupa P., Baumgardt H., 2008, *MNRAS*, 385, 1673
- Venemans B. P. et al., 2013, *ApJ*, 779, 24
- Vink J. S., de Koter A., Lamers H. J. G. L. M., 1999, *AAP*, 350, 181
- Vink J. S., de Koter A., Lamers H. J. G. L. M., 2000, *AAP*, 362, 295
- Vink J. S., de Koter A., Lamers H. J. G. L. M., 2001, *AAP*, 369, 574
- Volonteri M., Haardt F., Madau P., 2003, *ApJ*, 582, 559
- Volonteri M., Rees M. J., 2005, *ApJ*, 633, 624
- Wolcott-Green J., Haiman Z., 2011, *MNRAS*, 412, 2603
- Wolcott-Green J., Haiman Z., Bryan G. L., 2011, *MNRAS*, 418, 838
- Yoshida N., Omukai K., Hernquist L., 2007, *ApJ*, 667, L117

APPENDIX A: CONVERGENCE TESTS FOR NON-SPHERICAL INITIAL CONDITIONS

In Fig. 3, we have shown that despite the fragmentation present in higher resolution simulations, the mass contained in the central region of the central collapsing galaxy remains well converged. To improve on this point, we plot the phase space diagrams of density versus temperature at three different times for the $l_{\text{max}} = 20$ simulation in Fig. A1. The evolution is nearly identical to the $l_{\text{max}} = 19$ run which is shown in Fig. 2, and the main difference between these two simulations is caused by clump-clump interactions which affect the central structure. The structure of the cells we identify as star forming in the $l_{\text{max}} = 20$ simulation changes and becomes denser compared to the $l_{\text{max}} = 19$ run (see Fig. 5). We can test how these denser clumps affect the formation of VMSs by applying the same method for creating initial conditions as used in Section 3.1.1 to the highest resolution simulation.

In Table A1, we list the initial conditions and results of direct N -body simulation run using as input the $l_{\text{max}} = 20$ run. Even though these runs have slightly less mass, we find that f_{VMS} has increased due to the increase in density. Overall, M_{VMS} remains reasonably consistent with our previous results which suggest that this mass is robust.

APPENDIX B: VARYING THE STAR FORMATION EFFICIENCY

Most of our models were based on the assumption of an SFE of $\epsilon = 2/3$ which is motivated by a series of observations and simulations of relevant environments. We test two models where the SFE is changed and these models are listed in Table B1. The cluster parameters are derived using equations (4)–(7) and note that the initial central densities of the clusters are dependent on the chosen ϵ . We see that VMSs can form in clusters with lower M_* although they likely require higher central densities.

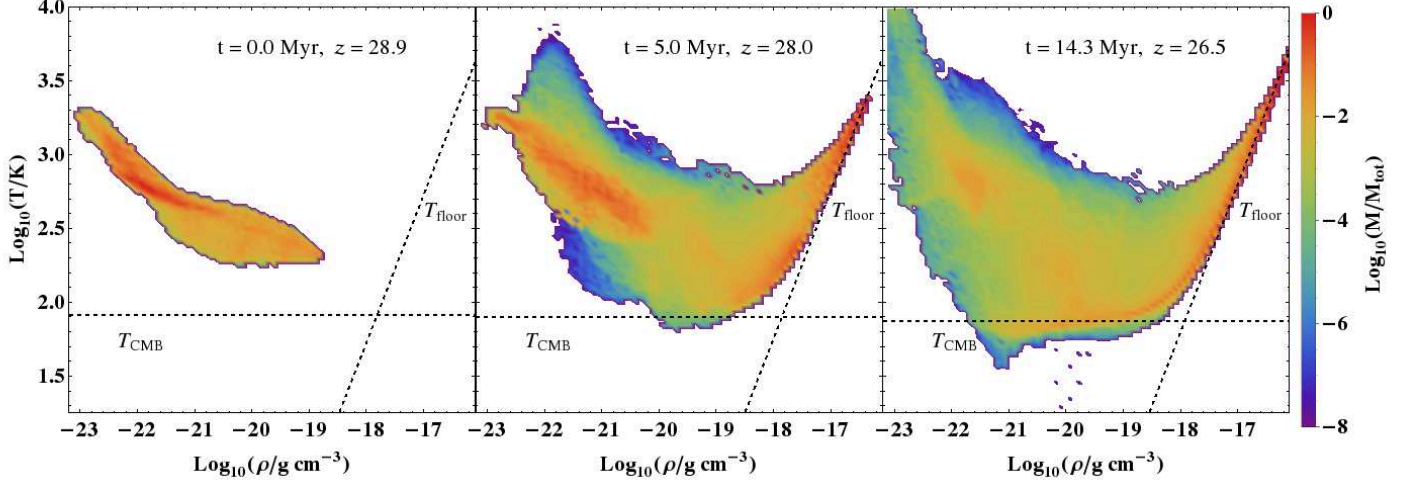


Figure A1. Mass-weighted phase space diagrams of density versus temperature at the initial collapse (*left*), 5 Myr after the collapse (*middle*), and 14.3 Myr after collapse (*right*). This includes all gas within 10 pc of the densest cell. The gas cools to a few hundred kelvin initially due to H_2 cooling then reaches the CMB temperature floor due to HD and metal cooling. The dashed lines represent the CMB temperature floor and the artificial temperature floor as labelled.

Non-Spherical Models: Convergence

Initial Conditions					Results							
ρ_{init}	IMF	Q	D	S	\bar{N}_{coll}	f_{VMS}	f_{PISN}	f_{NE}	\bar{M}_{seed} M_{\odot}	$M_{\text{VMS,max}}$ M_{\odot}	\bar{M}_{VMS} M_{\odot}	M_{SMBH} $10^9 M_{\odot}$
CD	TH_Salp	0.5	3.0	0.0	2.38	16.0 ± 5.7	46.0 ± 9.6	38.0 ± 8.7	87.6	311.8	290.4	2.91
CD	TH_Salp	0.3	3.0	0.0	2.40	18.0 ± 6.0	56.0 ± 10.6	26.0 ± 7.2	84.8	351.3	294.3	2.95
CD	TH_Salp	0.1	3.0	0.0	2.44	24.0 ± 6.9	32.0 ± 8.0	44.0 ± 9.4	89.0	349.0	296.6	2.98

Table A1. 50 Realizations of each model are generated. See Table 1 for definitions of the listed quantities.

APPENDIX C: ALTERNATIVE MODEL FOR MASS SEGREGATION

We generate one additional model in order to compare an alternative method for primordial mass segregation with the one we have used in the text in order to determine how sensitive our results are to the algorithm used. Here we adopt the algorithm of Šubr et al. (2008) and the results are listed in Table C1. For this model, we use the TH_Salp IMF and it is directly comparable with the model in Section 3.2 with the same IMF and initial degree of primordial mass segregation. Within the 1σ errors on the percentages of VMSs and PISNs that form, these models are entirely consistent suggesting that our choice of algorithm is not significantly affecting the results.

Spherical Models: Varying the Star Formation Efficiency

Initial Conditions			Results										
ϵ	M_* $10^4 M_\odot$	$R_{*,vir}$ pc	f_c	Q	D	\bar{N}_{coll}	f_{VMS} per cent	f_{PISN} per cent	f_{NE} per cent	\bar{M}_{seed} M_\odot	$M_{VMS,max}$ M_\odot	\bar{M}_{VMS} M_\odot	M_{SMBH} $10^9 M_\odot$
1/2	0.76	0.107	0.2	0.5	3.0	3.90	50.0 ± 10.0	40.0 ± 8.9	10.0 ± 4.5	84.1	492.8	345.8	3.47
1	1.52	0.215	0.2	0.5	3.0	4.40	45.0 ± 9.5	40.0 ± 8.9	15.0 ± 5.5	82.8	551.0	402.5	4.04

Table B1. 20 Realizations of each model are generated. See Table 1 for definitions of the listed quantities.**Spherical Models: Alternative Mass Segregation**

Initial Conditions		Results							
Profile	Parameters	\bar{N}_{coll}	f_{VMS} per cent	f_{PISN} per cent	f_{NE} per cent	\bar{M}_{seed} M_\odot	$M_{VMS,max}$ M_\odot	\bar{M}_{VMS} M_\odot	M_{SMBH} $10^9 M_\odot$
Subr	$S = 0.5$	3.92	50.0 ± 10.0	$36. \pm 8.50$	14.0 ± 5.3	84.4	559.5	350.3	3.51

Table C1. See Table 1 for definitions of the listed quantities.